12

H/D Effects of Water in Room Temperature Ionic Liquids

Hiroshi Abe[1] and Yukihiro Yoshimura[2]
[1]*Department of Materials Science and Engineering, National Defense Academy, Yokosuka 239-8686,*
[2]*Department of Applied Chemistry, National Defense Academy, Yokosuka 239-8686, Japan*

1. Introduction

In life science, the 3D structure, sequence and hyperstructure of biomolecules are summarized from the viewpoint of hydrogen bonding (Marechal, 2007). The bonding nature gives rise to network-forming, flexible, mobile and adjustable properties. As dynamic properties, 'function and structure' are affected directly or indirectly by hydrogen bonding. At different times and in different places, hydrogen bonding is variant, fluctuating and cooperative. In particular, a simulation study suggested that, in an inhomogeneous local circumstance, the dynamics of biomolecules are influenced by the hydration water (Kumar et al., 2006).

As we know, a variety of crystal structures of pure water can be induced by changing the bonding angle and the distance between water molecules under high pressure (Salzmann et al., 2009). The complicated phase diagram of water contains metastable phases. The simple molecular structure but complicated nature of water leads us to a significant finding: there exist at least two glassy states in water, the low-density amorphous ice (LDA) and the high-density amorphous ice (HDA), called polyamorphisms (Mishima & Stanley, 1998). This behavior is one of the entirely 'mysterious' properties of water. Moreover, the possibility of a liquid-liquid phase transition is noted, with hypothesized 'second' critical points. This phase transition may occur, for example, from a low-density liquid (LDL) phase at low pressure to a high-density liquid (HDL) at high pressure, and vice versa.

In this study, we focus on the 'hidden' behavior of water in room temperature ionic liquids (RTILs). RTILs consist only of a cation and an anion. Near-zero vapor pressure and nano-heterogeneity are representative features of RTILs. Both in previous experiments (Triolo et al., 2007) and molecular dynamics (MD) simulations (Jiang et al., 2007), the nano-heterogeneity was well explained by introducing polar and non-polar regions. In RTIL-H_2O systems, it was found experimentally that density fluctuations decrease with increasing H_2O concentration (Aono et al., 2011). In MD simulations of RTIL-H_2O mixtures (Jiang et al., 2007), as the water network develops with increasing H_2O concentration, the interrupted process of nano-heterogeneity is visualized in the simulation box. RTILs provide an appropriate electrostatic field such as the protein-water system in cells or membranes. In simple RTIL-water systems, ambiguous factors in the complicated protein-water system are

substantially decreased. Therefore, we can discover the role of water from the water-assisted functions in simple RTIL-water systems.

A the non-imidazolium RTIL, *N, N*-diethyl-*N*-methyl-*N*-(2-methoxyethyl) ammonium tetrafluoroborate, [DEME][BF_4], was selected for this study. In [DEME][BF_4]-water systems, an unusual geometrical effect is seen both in the liquid and solid states. In the liquid state, a 'hierarchy structure' (Aono et al., 2011) is formed at a specific water concentration. In the solid state, two kinds of superstructures, an anomalous domain structure and volume contraction, are observed only in 1 mol% H_2O mixtures. This anomaly is weakened by substitution of heavy water (D_2O) at the fixed 1 mol% concentration of water. Moreover, three different kinds of glassy states are obtained by slow cooling and rapid quenching. 'Nearly-free hydrogen bonded' (NFHB) water in the liquid state still exists in the rapidly quenched glassy state.

2. Hydrogen bonding: geometrical effects and proton dynamics

Generally, the hyperstructures of biomolecules are derived from multifunctional hydrogen bonding, which is mainly induced by water molecules. In such biomolecule-water systems, the bonding nature depends on the competition between geometrical effects and proton dynamics. In some circumstances, the competition between molecules is enhanced by the local charge balance, since charge imbalance is compensated for by geometrical effect or proton dynamics. Not only the local balance but also the stabilization of the system is realized by hydrogen bonding. The bonding network is optimized energetically through hydrogen bonding. Analogous with networks in synapses, the water-assisted system inherently possesses (i) information, (ii) information transfer (including feedback mechanisms), (iii) information selectivity (or switching mechanisms) and (iv) information memory.

Many studies associated with proton dynamics have been carried out in the crystal state, since degrees of freedom are reduced in crystal systems. For instance, the 'bonding structure' of carboxylic acid-based crystals is summarized in a previous study (Foces-Foces et al., 2001). The bonding length of hydrogen bonding is responsible for degenerate double proton transfers between O-H···N and O···H-N. In addition, a proton order-disorder transition is observed directly by NMR measurements. Generally, the hydrogen bonding network consists of dimers, trimers, tetramers and higher molecular sequences. An amorphous solid is formed by curved or *zigzag* molecular sequences as a disordered state, while a linear molecular sequence contributes to the crystal structure. Consequently, a scenario describing the formation of crystals or amorphous solids is provided by the 'hierarchy structure' (Fig. 1): (i) on the atomic scale, proton dynamics are derived from the local environment, (ii) on the mesoscopic scale, a variety of molecular sequences are induced by hydrogen bonding. Here, we have a big question: why can proton dynamics govern the molecular network to determine whether the crystal or amorphous solid is stabilized? To answer this question, the hydrogen/deuteron (H/D) effect was investigated as another approach. For instance, proton dynamics are drastically changed by deuteron replacement. It should be noted that the H/D effect is not simply a mass effect. In solid state NMR methods, intermolecular multiple proton-transfer processes were explained by H/D isotope effects (Klein et al., 2004). The kinetic behaviors of the double proton and deuteron transfer in the solid state are well described by the Bell-Limbach tunneling model.

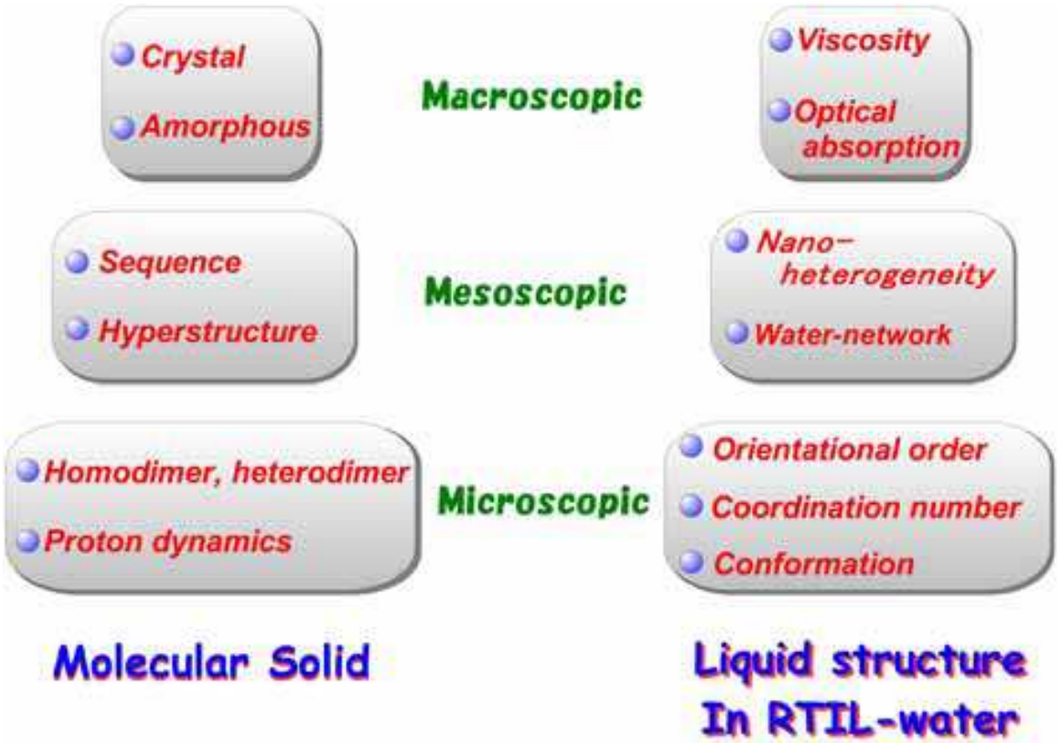

Fig. 1. Hierarchy structure in a molecular solid and RTIL-water system in the liquid state.

A part of the universal aspect of biochemistry is also seen in ferroelectric materials. Well-ordered molecular ferroelectric materials, whose charge is highly balanced in the lattice, can minimize their positional, orientational and conformational ambiguity, apart from protons. Therefore, proton dynamics are enhanced in the 3D network. The 'giant isotope effect' on hydrogen bonds is one example describing spatially restricted protons or deuterons. For instance, potassium dihydrogen phosphate (KH_2PO_4) and its deuterated compound (KD_2PO_4) have quite different phase transition temperatures, T_c. The T_c of KH_2PO_4 is around 122 K, while that of KD_2PO_4 is 229 K. DFT (density functional theory) calculations indicate the atomic positions of hydrogen: the on-centering of H (O-H-O) and the off-centering of D (O···D -O) (Koval et al., 2002). This centering can determine the bonding length, which is regarded as a 'geometrical effect'. The distances between oxygens, d_{OO}, are estimated to be 0.242 nm (H) and 0.251 nm (D), respectively. The quantum delocalization of the proton contributes to the attractive interaction, that is, the 'proton-mediated covalent bonding' (PMCB). As a geometrical effect, below T_c, the off-centering of proton induces positional shifts of the P and K ions to stabilize the total energy. In further *ab initio* calculations of KH_2PO_4 and KD_2PO_4 (Koval et al., 2005), it was pointed out that proton motions are strongly correlated with the heavier ions within clusters in addition to the geometrical effect. The feedback effect of the geometrical modifications can explain not only the isotope effect but also the phase transitions under pressure. Further *ab initio* calculations introducing two different kinds of cluster models (Lasave et al., 2005) suggest that rotational defects of PO_4 cause a lattice contraction in KH_2PO_4. Domain wall motion around the domain freezing temperature, T_F (=T_c-60 °C), is connected with a polarization flip. Both the domain wall and polarization dynamics are controlled extensively by the proton motion.

3. Experimental and calculation methology

3.1 Materials

As the sample RTIL in this study, we used *N, N*-diethyl-*N*-methyl-*N*-(2-methoxyethyl) ammonium tetrafluoroborate, [DEME][BF_4] (Fig. 2) (Kanto Chemical Co., Tokyo, Japan), which is a hydrophilic RTIL (Sato et al., 2004). The as-received sample contains a small amount of water (126 ppm). Generally, RTILs are easily contaminated by vacuum drying to reduce H_2O, so we used the sample without further purification. Mixtures were prepared by dissolving RTILs in a dry box, under a flow of He gas to exclude atmospheric H_2O. The amount of water was estimated on the basis of the Karl-Fischer titration method. Special care was taken not to contaminate chemicals further with atmosphere. For H_2O mixtures, distilled water (Wako Pure Chemical Co. Japan), was used, while D_2O (99.9%) (Cambridge Isotope Laboratories, Inc.) was used for D_2O mixtures. H_2O concentrations, x, ranged from 0.0 to 98.5 mol% H_2O. H_2O-D_2O mixtures are represented as (1-y)H_2O·$y D_2O$. Sample solutions were prepared simply by dissolving the required amounts of water in [DEME][BF_4] in the dry box filled with He gas.

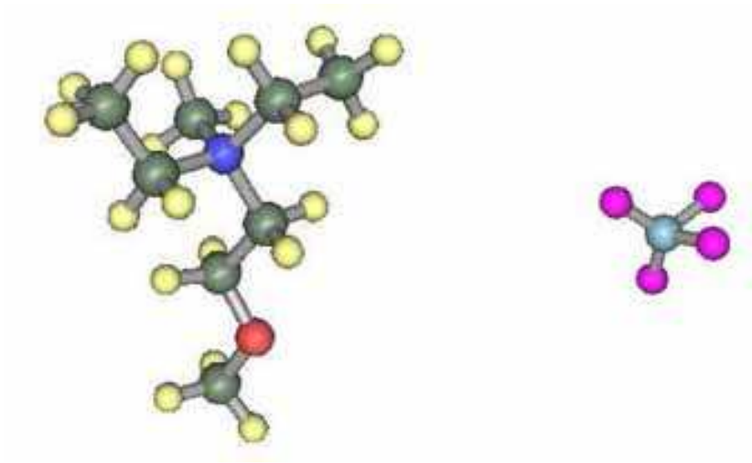

Fig. 2. Molecular structures of the cation [DEME] and the anion [BF_4].

3.2 Simultaneous wide angle X-ray scattering and differential scanning calorimetry measurements

In-situ observations were performed using a simultaneous wide angle X-ray scattering (WAXS) and differential scanning calorimetry (DSC) (RINT-Ultima III; Rigaku Co., Tokyo, Japan), where the DSC is attached on a vertical goniometer. For in-situ observations of the liquids, the sample stage is fixed horizontally. The sample is put on an Al sample holder inside the DSC. A sealed X-ray tube (2 kW) and a scintillation counter move simultaneously. A parallel beam is obtained by a parabolic multilayer mirror. A long Soller slit is placed in front of the scintillation counter. Cu Kα radiation (λ=0.1542 nm) was selected for the simultaneous measurements. Beam divergence with the beam optics is estimated to be 0.1° by measuring a standard Si polycrystal. DSC windows for X-ray are metal coated Mylar films. During the simultaneous measurements, dry N_2 gas was flowing at 20 cc/min in order to reduce moisture.

In this study, two kinds of scan modes, θ-2θ and θ scans, were carried out. For conventional WAXS, a θ-2θ scan was used. The θ-2θ scan mode is the radial scan in reciprocal space. Peak

shifts and widths along the radial scan contain information of lattice distortions. The direction of the θ scan (rocking curve) is transverse to the radial direction in reciprocal space. The θ scan can detect the preferred orientation on the Debye ring of polycrystalline structures and mosaicity of a single crystal. Peak widths along the transverse direction contain information of crystal domain formation. The θ scans are performed by asymmetric movement of the X-ray tube and counter, while the sample stage is held horizontal. Crystal structures and precise lattice constants are determined by JADE application software (Rigaku Co.).

3.3 Conventional WAXS and small angle X-ray scattering

At room temperature, WAXS and small angle X-ray scattering (SAXS) of the liquid state were measured using an 18 kW X-ray generator (RINT2500; Rigaku Co., Tokyo, Japan). Cu Kα radiation was selected for both WAXS and SAXS. Scattered intensity was monochromated for WAXS by curved highly oriented pyrolytic graphite (002). Transmission geometry of the sample was set for both measurements. Windows for the sample holder were made of 7.5 μm thick polyimide thin films (Kapton; Nilaco Co., Tokyo, Japan). Using step scan mode at a fixed intervals, a few thousand counts were collected even at high scattering angles for both the sample and the background. Instead of the monochromator, Ni filter was set to decrease Kβ in the SAXS. The beam divergence in SAXS was 0.052°. DATA were collected above 0.2° in 2θ. A vacuum path was placed between the sample and the scintillation counter in order to reduce air scattering.

To analyze the WAXS patterns quantitatively (electron units per molecule), we measured several integrated intensities of a standard powdered sample of Ni (Abe et al., 2007a). The calculated Compton scattering was subtracted from the corrected WAXS patterns. Here, the scattering vector, Q, is defined to be $4\pi(\sin\theta)/\lambda$ (nm^{-1}). The radial distribution function (RDF) is given by (Nishikawa & Iijima, 1984; Katayanagi et al., 2004),

$$4\pi r^2\left(\rho-\rho_0\right)=\frac{2r}{\pi z^2}\int_0^\infty Qi(Q)\sin(Qr)\,dQ\,. \tag{1}$$

z^2 is provided by $z^2=\sum_n {z_n}^2$, where z_n is the atomic number of the nth component atom.

In SAXS analysis, the Ornstein-Zernicke (OZ) correlation function (Stanley, 1971), $\chi(r)$ is introduced by analyzing critical scattering. The correlation function is given by,

$$\chi(r)=\frac{1}{r}e^{-r/\xi}\,, \tag{2}$$

where ξ is the correlation length. By Fourier transform of Eq. (2), the SAXS intensity using the OZ correlation function is obtained as $I_0/(1+\xi^2Q^2)$. By modifying the equation, ξ is calculated from a plot of Q^2 vs. $1/I(Q)$.

3.4 Conventional DSC and differential thermal analysis measurements

Conventional DSC experiments were also carried out using DSC2910 (TA Instruments Japan Co., Tokyo, Japan) to ensure the complete phase behavior, cooling or heating rate dependence of the phase transitions was examined at 2, 4, 8, 9 and 10 °C/min, respectively. Thermal cycle experiments without replacing the sample were also performed repeatedly from 20 to -150 °C.

A simple differential thermal analysis (DTA) system designed for rapid quenching experiments was employed. As a reference material for the measurements, benzene (Wako Pure Chemical Co., Japan) was used. A sample cell (about 35 mm long and 2 mm i.d. glass tube with one side sealed) was filled with a mixture, and then a thermocouple junction was placed 25-30 mm from the mouth of the sample cell. As a precooling procedure, a vitrification was done by putting the whole sample solution directly into liquid nitrogen (500 °C/min). After removing the sample from the liquid nitrogen, the DTA traces were recorded.

3.5 Raman spectroscopy and optical absorption measurements

Raman spectra were measured by a NR-1800 Raman spectrophotometer (JASCO Co., Tokyo, Japan) equipped with a single monochromator and a CCD detector. The 514.5 nm/line from a Lexel Ar^+ ion laser was used as an excitation source with a power of 250 mW. The Raman spectra were measured in the OH-stretching vibrational region for water along with the CH-stretching band of [DEME] cation. Using a THMS-600 (Linkam Co., UK) temperature controller, the sample temperature was controlled between room temperature and -100 °C. Both the cooling and heating rate was 5 °C/min.

The optical absorption spectra were measured using a ultraviolet and visible (UV-vis) spectrometer (V-570; JASCO Co., Tokyo, Japan) with a 1 cm path length quartz cell. All the measurements were performed at room temperature.

3.6 DFT calculation

DFT calculations were used as the investigation methodology for the interactions between the RTIL and water molecules (Zhang et al., 2008; Danten et al., 2010). Here, we performed DFT calculations on the optimized arrangement of the $BF_4^-\cdots n(H_2O)$ complexes (n=1-4, where n is the number of H_2O) to investigate the interaction between the BF_4^- anions and water molecules. All DFT calculations were carried out using the Gaussian03 program (Frish et al., 2003). For calculations on the $BF_4^-\cdots n(H_2O)$ complexes, we used Becke's three-parameter (B3) exchange function (Becke, 1988). The B3 exchange function was combined with the Lee-Yang-Peer correlation function (B3LYP) (Lee, 1988). All calculations by this method were performed using the 6-311++G(d,p) basis set.

4. Experimental results and discussion

4.1 Phase stability of solid

Examples of simultaneous WAXS-DSC measurements are shown in Figs. 3(a) and 3(b). WAXS on cooling reveal broad diffraction patterns due to the amorphous solid of [DEME][BF_4] at 60.5 mol% H_2O (Fig. 3(a)). Crystallization of [DEME][BF_4] is completely suppressed even upon slow cooling (8 °C/min), although quite weak but sharp Bragg reflections from ice crystals of H_2O were detected in the broad diffraction pattern. The green triangles in Figs. 3(a) and 3(b) are calculated 2θ values of the ice crystal. The red circle is an ideal peak position of the Bragg reflection, which is identified as an Al sample holder. At the same time, corresponding phase changes at 60.5 mol% H_2O were obtained from the DSC thermograph as shown in Figs. 3(a) and 3(b). On cooling, small exthothemal peaks, which are derived from the ice crystallization temperature (T_I) and glass transition temperature of [DEME][BF_4] (T_g), were observed. The T_I and T_g lie very close together. By systematic

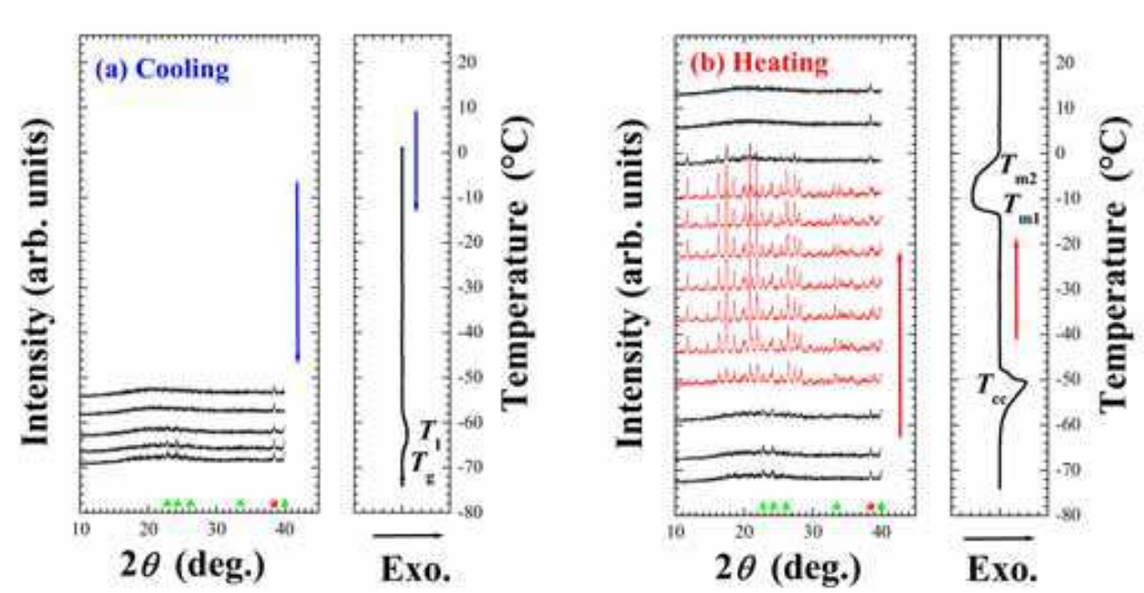

Fig. 3. Wide angle X-ray scattering (WAXS) of [DEME][BF_4]-H_2O mixture at 60.5 mol% H_2O both on (a) cooling and (b) heating. On cooling, an amorphous solid of [DEME][BF_4] is formed at low temperature and a small amount of H_2O ice crystals appears below -60 °C. Closed green triangles and red circles indicate the calculated 2θ values of Bragg reflections of H_2O ice crystals and the Al sample holder, respectively. DSC thermograms of the [DEME][BF_4]-H_2O mixture at 60.5 mol% H_2O are plotted along with the WAXS. A weak exothermal peak is observed on cooling. The glass transition of [DEME][BF_4] (T_g) and crystallization of a small amount of H_2O ice crystal (T_l) occur simultaneously. On heating, 'cold crystallization' of [DEME][BF_4] is observed at T_{cc} accompanying the exotherm. Additionally, two kinds of melting points, T_{m1} and T_{m2}, are observed.

measurements, we found that ice crystals of H_2O (I-phase) exist above 60 mol% (x_l). Upon heating, the distinct exothermal peak at -60 °C (T_{cc}), which is due to 'cold crystallization', appears on the thermograph. This is in accordance with the appearance of Bragg reflections in WAXS on heating as shown in Fig. 3(b). By further heating, the crystal melts with two endotherms characterized by two stages of melting, at T_{m1} and T_{m2}, which are caused by two kinds of crystal structures in the system (Imai et al., 2008a). By simultaneous WAXS-DSC measurements, we can successfully determine the T_c, T_l, T_g, T_{cc}, T_{m1} and T_{m2} experimentally. Here, we define the normal crystallization temperature of [DEME][BF_4], T_c. A variety of phase behaviors both on cooling and heating is shown in Figs. 4(a) and 4(b), respectively (Abe et al., 2009). Since the diagrams obtained in this study may depend on the cooling and heating rates, here we tentatively call these 'kinetic phase diagrams'. Closed circles in the 'kinetic phase diagrams' indicate the phase transitions observed by the simultaneous WAXS-DSC measurements. L indicates the liquid phase. First, we explain the results of the downstroke direction on cooling (Fig. 4(a)). From the experimental facts, we find that the crystal phase of [DEME][BF_4] (C-phase) exists only for a small range of water content ($0<x<4$ mol%). The crystallization temperature of [DEME][BF_4], T_c, decreases with increasing water concentration. At 4-10 mol%, pure amorphous phase (A-phase) appears. The slow-cooled glass is described in detail in the next section. A two-phase coexistence, the (A+C)-phase, is

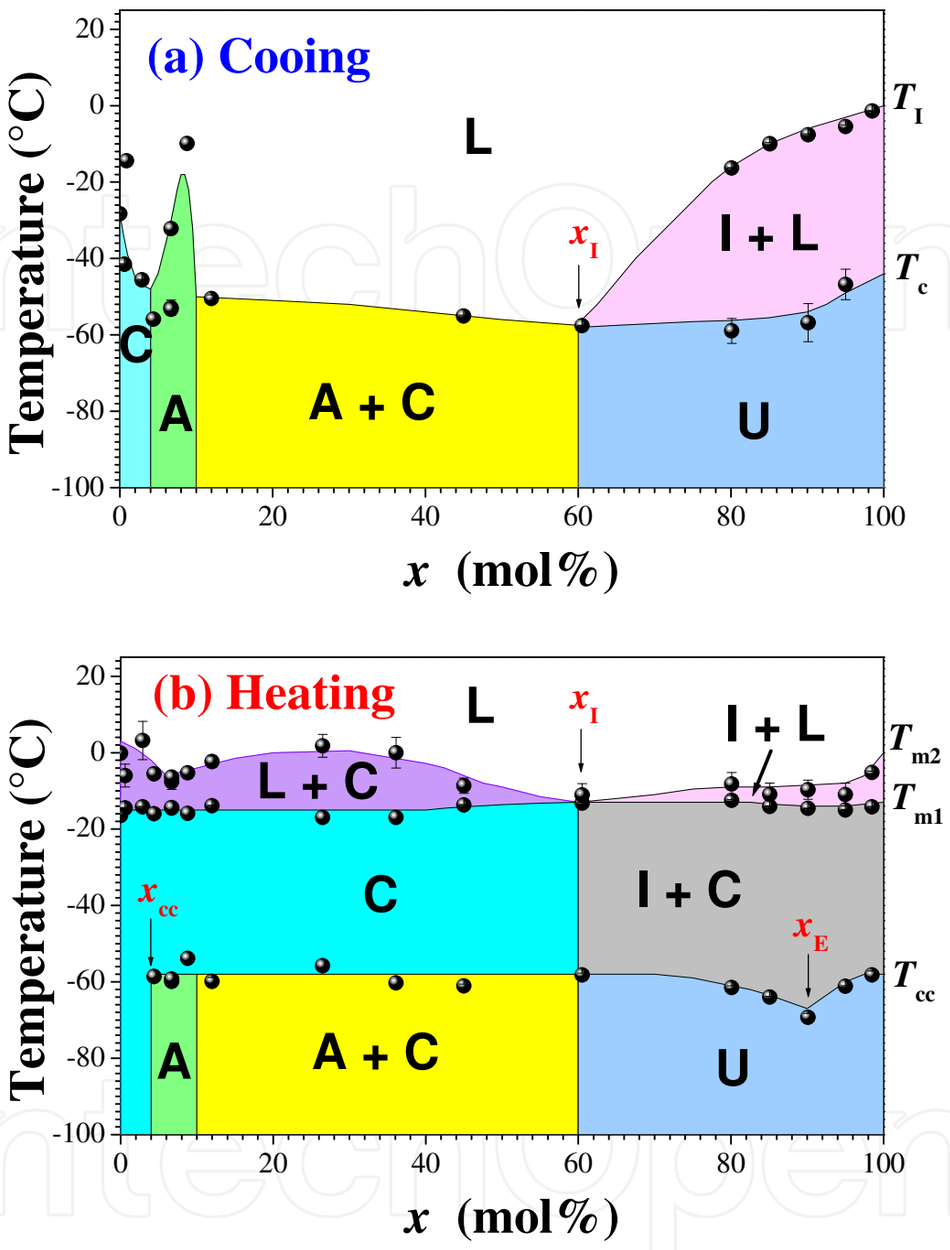

Fig. 4. 'Kinetic phase diagrams' of [DEME][BF_4]-H_2O mixtures on (a) cooling and (b) heating. Closed circles represent observed data, which are determined by simultaneous WAXS-DSC measurements. x_{cc} and x_I are defined to be a critical concentration of the 'cold crystallization' and the formation of H_2O ice crystal, respectively. T_{cc} is the 'cold crystallization' temperature with an exothermal peak on heating. T_{m1} and T_{m2} are the melting temperatures, respectively. L, C, A, I and U represent the liquid, [DEME][BF_4] crystal, amorphous, H_2O ice and undefined phases. U is classified further into (I+A)-, (I+C)- and (I+A+C)-phases.

realized from 10 to 60 mol%, whereas a coexistence of the A-phase of [DEME][BF_4] and H_2O ice crystals (I-phase) is formed at x_I (=60 mol%). Here, we define the temperature T_I as the crystallization temperature of H_2O ice. In contrast to T_c, the T_I of the ice increases gradually with increasing water concentration. At $x>x_I$, another interesting feature is found. The solid phase of the mixture of [DEME][BF_4]-H_2O is hardly uniquely defined in this region. U represents undefined phases. That is, despite using the same sample and cooling rate, the same solid phase did not appear in a reproducible manner. Here, three kinds of phases, classified as (i) (I+A)-, (ii) (I+C)- and (iii) (I+A+C)-phases, appear randomly.

4.2 Comparison of the slow-cooled and quenched glasses

Despite a normal cooling rate (1-10 °C/min), A-phases appeared in specific regions ($4<x<10$ mol% and x=60 mol%) as shown in Fig. 4(a). The T_g of the A-phase at 6.7 mol% depends on cooling rate systematically, though T_c of the pure [DEME][BF_4] is almost constant (Imai et al., 2008a). The slow-cooled glass at 6.7 mol% is characterized by 'two dynamic components' in its Raman spectra. These spectra were measured at -80 °C ($T < T_c$), apart from the spectra of the liquid states at 6.7 and 60.1 mol% H_2O, which were obtained at 25 °C in order to compare with the Raman spectra in the slow-cooled glasses. The Raman spectra in the region of 2700-3200 cm^{-1} (Fig. 5(a)) concern the CH stretching vibrational mode of the cation. The signal at 680 cm^{-1} (shown in Fig. 5(b)) is assigned to the C_4N symmetric modes of the cation (Imai et al., 2008a) and the signal at 740 cm^{-1} is in the BF_4 stretching region. The Raman spectrum of the slow-cooled glass (x=6.7 mol%) is similar to that of the crystal (Fig. 5(b)). In contrast, the Raman spectrum at around 3000 cm^{-1} (CH-stretching vibrational region of the cation) is almost the same as that of the liquid phase. The crystal-like and liquid-like spectra are emphasized as 'two dynamic components', although no difference between the liquid and the slow-cooled glass (x = 6.7 mol%) was observed in WAXS.

Apart from the slow cooled glass ($4<x<10$), at around 60 mol%, a 'competitive glass' is generated as a crossover point from [DEME][BF_4]-based to H_2O-based properties. Basically, the competitive glass is similar to a spin glass, described as a locally frustrated system. In some cases, the frustration is caused by a competition between ferro-like and antiferro-like interactions (Satoh et al., 1978). In fact, crystallization of the mixture is completely suppressed at 60.1 mol%, apart from a small amount of ice crystallization as shown in Fig. 3(a). In the Raman spectra both at low and high bands, the profile of the 60 mol% glass is similar to that of the liquid at 60.1 mol% (Figs. 5(a) and 5(b)).

This implies that the 'two dynamic components' seen in the 6.7 mol% glass were not seen at 60.1 mol%. On the other hand, a similarity between them is that 'nearly-free hydrogen bonded' (NFHB) water disappeared upon solidification in both cases. NFHB water is described in the following section.

Although glassy states are realized even by slow cooling processes, we performed rapid quenching experiments. By DTA measurements, T_g varied extensively with the water concentration (Fig. 6) (Imai et al., 2010). On heating, pure [DEME][BF_4] shows a glass transition at -100 °C. Rapid quenching prevents the pure [DEME][BF_4] from crystallizing below T_c. Above T_g, the melted liquid from metastable glass was crystallized by further heating (T_{cc}=-74 °C). Since pure [DEME][BF_4] has no 'cold crystallization' on slow cooling, the quenched glass of pure [DEME][BF_4] is regarded as a highly non-equilibrium state. A significant finding in the quenched mixtures is that a double glass transition occurs at $16<x<30$ mol% (Imai et al., 2010). For instance, at x=18.1 mol%, a first glass transition was

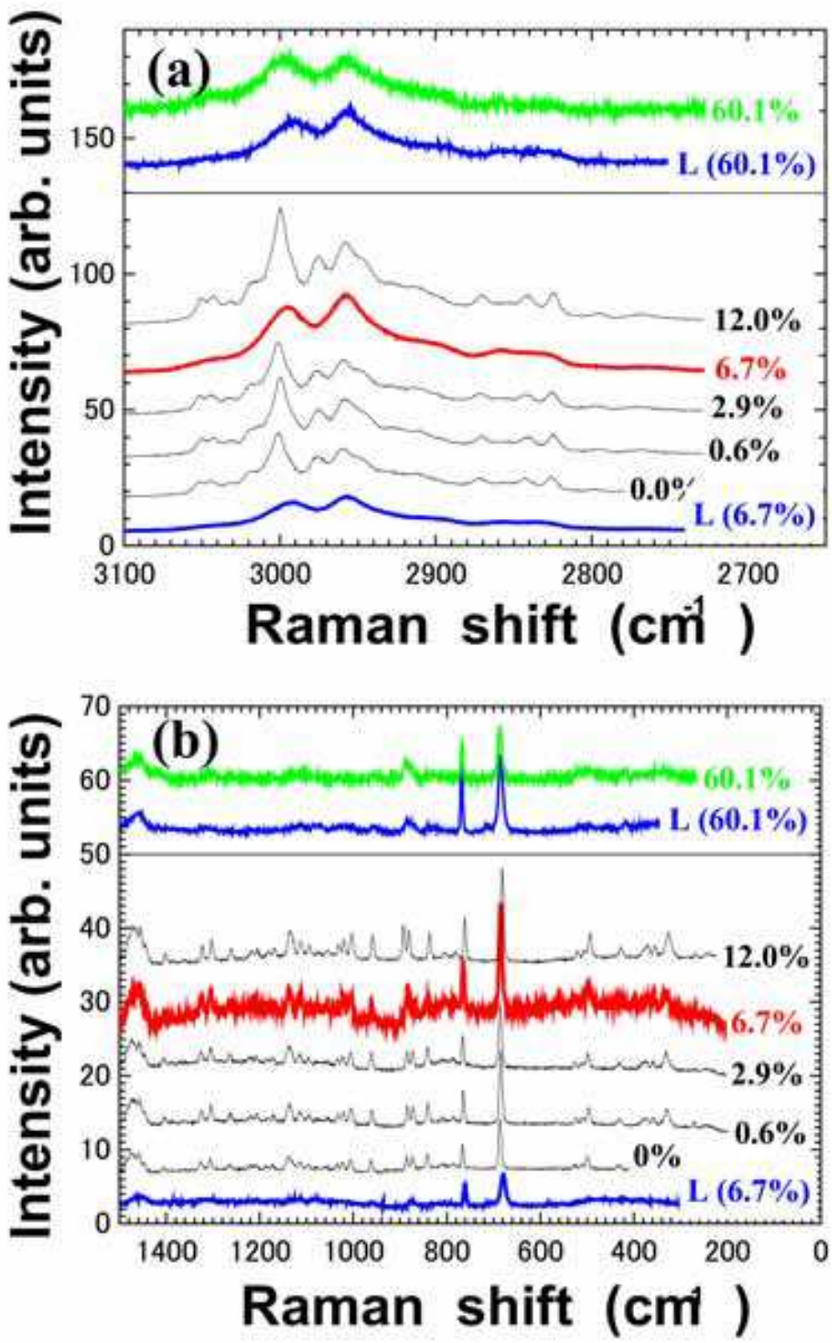

Fig. 5. H_2O concentration dependence of Raman spectra for [DEME][BF_4]-H_2O mixtures in the regions of (a) 2700-3200 cm^{-1} and (b) 200-1500 cm^{-1}. Raman spectra of the liquid state (6.7 and 60.1 mol%) were measured at 25 °C for a comparison with the slow-cooled glasses. Other Raman spectra were observed at -80 °C. The slow-cooled glass at 6.7 mol% H_2O provides two kinds of dynamic properties: liquid-like behavior around 3000 cm^{-1} and crystal-like behavior around 1000 cm^{-1}. In contrast, the other slow-cooled glass at 60.1 mol% has no crystal-like spectrum.

detected at around -100 °C (=T_{g1}) by an exothermic peak on the DTA trace. A second glass transition was carefully checked by re-quenching the sample (Imai et al., 2010). The second glass transition temperature, T_{g2}, is found to be around -95 °C. Finally, the metastable mixture is stabilized at -100 °C by 'cold crystallization' in the same manner as other water-rich regions with a single glass transition. Here, we predict that a new heterogeneous region, which is different from polar and non-polar heterogeneity (Triolo et al., 2007; Jiang et al., 2007), is formed by rapid quenching. One reason for this is that, in the liquid state, SAXS intensity in [DEME][BF_4]-H_2O decreased at 16<x<30 mol% (Aono et al., 2011). Simply, we consider that the new heterogeneity is explained by the difference in hardness, since the melting point is roughly proportional to the interaction between molecules. The soft part melts at T_{g1} and the relatively hard part melts at T_{g2}. As shown in Fig. 6, the T_{g1} of [DEME][BF_4]-H_2O mixtures look likely to be connected with the T_g of the water-poor region, while the T_{g2} curve is linked continuously with the T_g of the water-rich region. Therefore, in [DEME][BF_4]-H_2O, we suppose that the coexisting water-rich and water-poor regions are permitted from 16<x<30 mol% to change continuously from water-poor to water-rich regions. The water-poor region corresponds to the soft region and the relatively hard region is generated by the water-rich region. Very recently, in other RTILs, we found multiple glass transitions in [DEME][I]-H_2O (Imai et al., 2011) and [C_4mim][BF_4]-H_2O (Yoshimura et al., 2011). Here, [C_4mim][BF_4] is 1-butyl-3-methylimidazolium tetrafluoroborate. Generally, a series of cations such as 1-alkyl-3-methyl imidazolium is expressed by [$C_n$mim] where n is the the alkyl chain length.

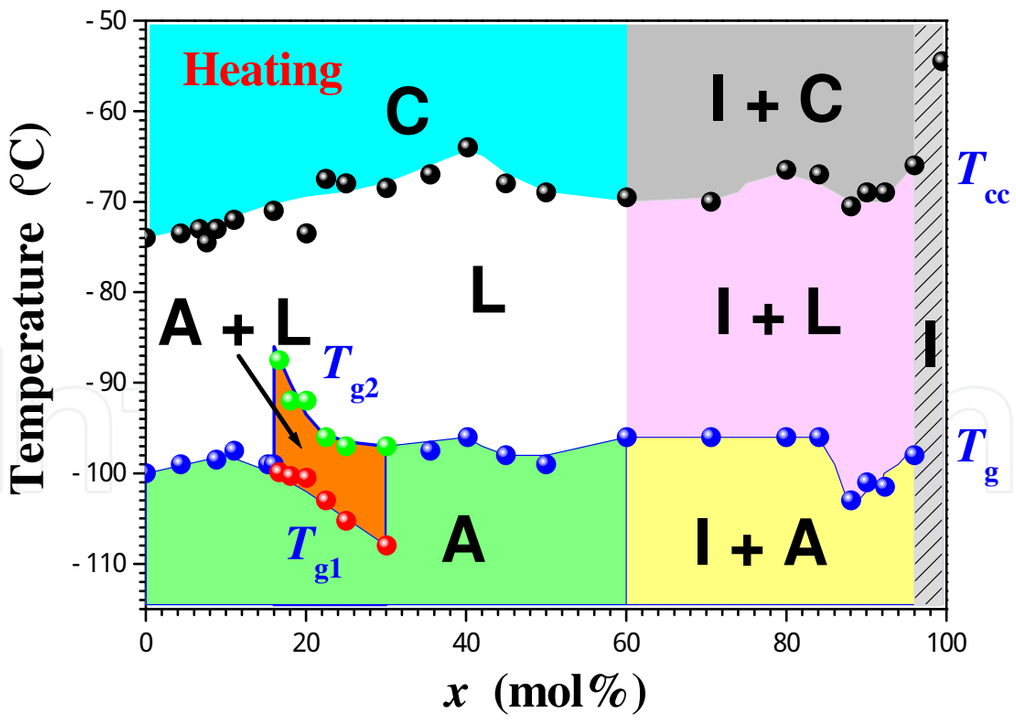

Fig. 6. T_g variations with H_2O concentration, x, in a quenched glass on heating.

In other systems, double glass transitions have already been reported. For instance, the double glass transition phenomenon in aqueous tetraalkylammonium halide solutions is

derived from a metastable liquid-liquid immiscibility (Kanno et al., 1983). It is interpreted that the homogeneous solution at room temperature is separated into a water-rich phase and a salt-rich phase by lowering its temperature. In comparison with the previous instances of double glass transitions, the following differences in glass transition behavior appeared in the [DEME][BF_4]-H_2O mixed solutions. For one thing, the glass-forming composition region of [DEME][BF_4]-H_2O mixtures is much wider than those of aqueous solutions of tetraalkylammonium halides (91-94 mol% H_2O). Also, the difference between the two glass transitions, ΔT_g (=T_{g2}-T_{g1}), is at most 15 °C, and this is much smaller than that of glycerol-H_2O mixtures (ΔT_g=90 °C) (Inaba & Andersson, 2007). In general, domain dynamics in multiple phase transitions are described by density and the domain boundary, size and elasticity, which are related to differences of enthalpy and phase transition temperature, ΔT. Therefore, we deduce that the small ΔT_g in [DEME][BF_4]-H_2O reflects the small difference in density (between the water-rich and water-poor regions) and its fluctuation size.

Another significant point in the quenched mixture is that ice crystals were observed in the Raman spectra above 60 mol%, in the region denoted by I in Fig. 6. Figure 7 shows the Raman spectra of the quenched mixtures at -196 ˚C. The OH stretching mode of the ice crystal is indicated by the arrows in Fig. 7. The appearance of ice in the quenched mixtures coincides with the water concentration in the slow-cooled solid (Fig. 4(b)). This means that excess water molecules tend to form conventional hydrogen bonds as in bulk water above 60 mol% at any cooling rate, though the extent strongly depends on the cooling rate.

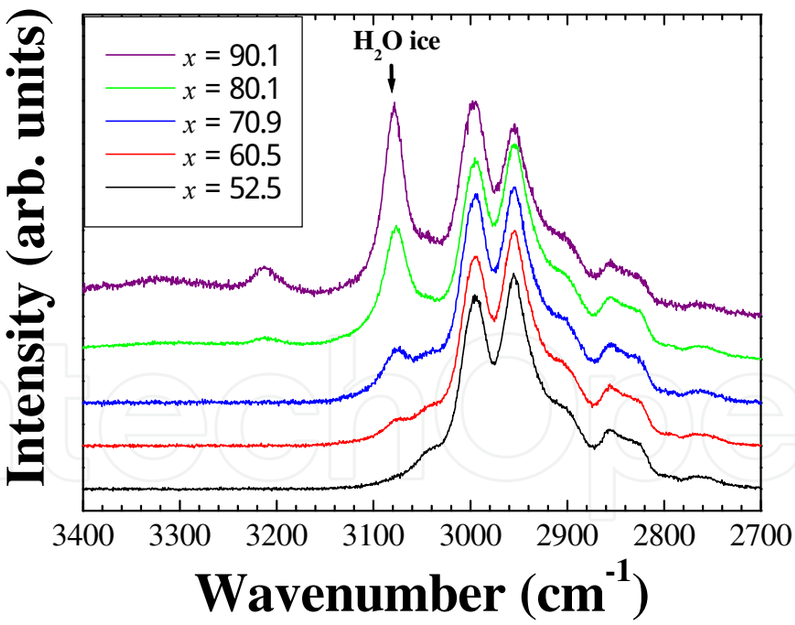

Fig. 7. Raman spectra in a quenched glass. Above 60 mol% H_2O, ice crystals appeared.

4.3 Nearly-free hydrogen bonding in liquid and quenched glass

Now, we have a big question: excess water molecules with bulk water properties cannot exist below 60 mol% in the solid state. The idea of a confined water molecule may be the key to resolving this problem. It should be noted that the Raman signal at around 3650 cm^{-1},

which is assigned to 'nearly-free hydrogen bonded' (NFHB) water molecules, exists below 80 mol% in the liquid state (Yoshimura et al.,2009). NFHB water means single molecules that do not form a hydrogen bonding network. In the quenched glass, NFHB water was observed at -196 °C in quenched mixtures below 80 mol% (Yoshimura et al.,2009). The entirely opposite tendency is seen in the slow-cooled glasses. Typically, the NFHB bands at 6.7 and 60.1 mol% (A-phase) seem to disappear at around -80 °C on slow cooling, as shown in Figs. 8(a) and 8(b). Theoretically, a picture of NFHB water can be simply visualized by DFT calculations (Abe et al., 2010a). Since H···F bonding between BF_4^- and H_2O is relatively strong, a $BF_4^-\cdots n(H_2O)$ (n=1-4) cluster is preferred (Figs. 9(a), 9(b), 9(c) and 9(d)). Certainly, Raman bands calculated by DFT are in good agreement with the observed spectra. If we take into account fully connected F (BF_4^-:H_2O=1:4), it is natural that bulk water tends not to appear at x < 80 mol %. The picture in the liquid state does not contradict the existence of NFHB water below 80 mol%. However, the population of the NFHB water in 60-80 mol% is estimated to be relatively small in the liquid state (Abe et al., 2009). Thus, on solidification both of slow cooling and rapid quenching processes, quite a small amount of ice crystals appears above 60 mol%.

We summarize three different glassy states as shown in Fig. 10. It is found that the three glasses are formed at specific water concentrations by slow cooling (SC) and rapid quenching (RQ) in the [DEME][BF_4]-H_2O system. The three types are classified as (i) 'two dynamic components' (SC), (ii) a crossover from RTIL to water (SC) and (iii) NFHB assisted-glasses (RQ). In the liquid state, nano-heterogeneity, which is separated into polar and non-

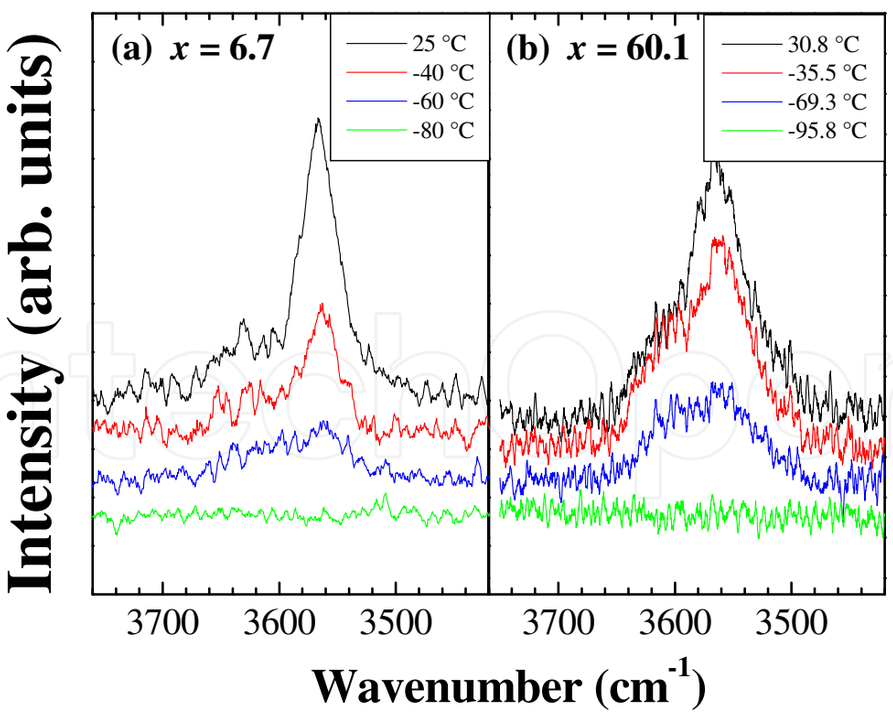

Fig. 8. Spectral changes in the nearly-free hydrogen bonded band of [DEME][BF_4]-H_2O at (a) x=6.7 mol% and (b) x=60.1 mol% by slow cooling.

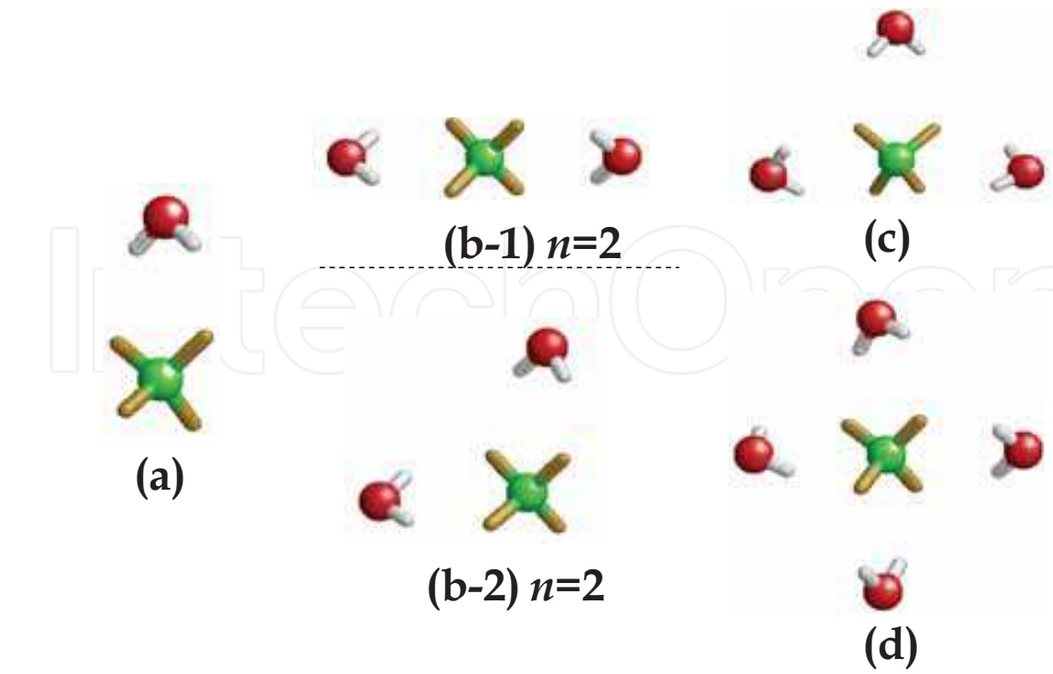

Fig. 9. Optimized structures of the $BF_4^-\cdots n(H_2O)$ (n=1-4) complex using the B3LYP/6-311++G(d,p) basis set. In the case of the $BF_4^-\cdots 2(H_2O)$ complex, the BF_4^- anion takes two arrangement patterns with two water molecules: one is a linear arrangement (b-1) and another is a perpendicular arrangement (b-2). The former is energetically more stable than the latter (ΔE=1.6 kJ/mol).

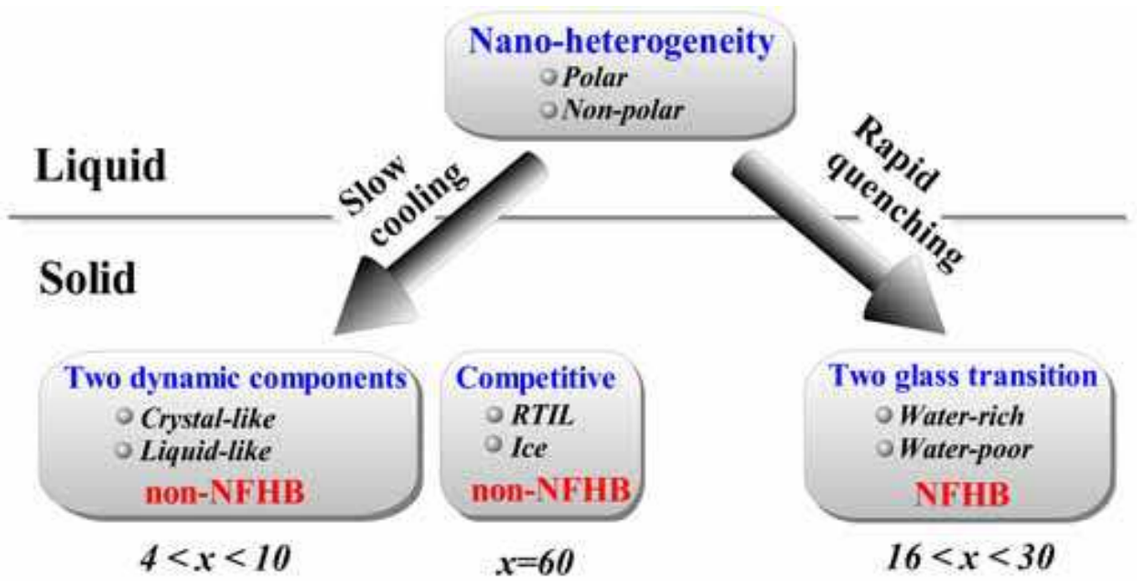

Fig. 10. Three glassy states in the [DEME][BF_4]-H_2O system. The existence of a nearly-free hydrogen bonded (NFHB) band of water implies that glass-forming mechanisms are different to each other.

polar parts, is stable in satisfying a charge balance. In the quenched glass, the double glass transition at 16-30 mol% suggests water compositional modulation (water-rich and water-poor). Supposedly, the T_{g1} and T_{g2} splitting corresponds to soft and hard glasses. NFHB water still exists even if some local diffusion to the modulation is permitted in rapid solidification. In contrast to this, the slow-cooled glass at 6.7 mol% is formed under a competition between liquid and crystal. The experimentally obtained 'two dynamic components' suggest that the local environment is decomposed into soft (liquid-like) and hard (crystal-like) parts. At the crossover point (60 mol%), the absence of the 'two dynamic components' suggests that the crossover-type glass appears simply as an intermediate state. Finally, we emphasize that the glass-forming mechanism is entirely different in the three glasses.

4.4 H/D effects at 1 mol% water mixture

As mentioned earlier, intensity modulation on the Debye ring connects with the crystal domain structure, which reflects on nucleation and growth processes. In crystallization, a highly preferred orientation on the Debye ring was observed in [DEME][BF_4]-0.9 mol% H_2O (Fig. 11(a)) (Imai et al., 2008b). Rocking curves (θ scan mode) in the [DEME][BF_4]-water mixtures are obtained at a fixed 2θ value (17.4°). The full width at half maximum (FWHM) of the peaks is estimated to be around 0.2°, where the mosaicity is equivalent to that of a single crystal. Moreover, each peak has a specific orientational relation of twin-crystal structure, such as can be observed in a shape memory alloys (Abe et al., 1994). A twinlike structure is represented by a pair of peak splittings. At 0.6 mol% and just below 1 mol%, the distinct sharp peaks vanished but broad modulations of intensity remained on the Debye ring. This is typical or preferred orientations as seen in conventional microdomains, which have weak orientational relationships. However, the preferred orientation disappears completely above 2.9 mol%. The ideal Debye ring show fairly fine domains or particles are randomly located with little orientational correlation to each other. Considering the conventional domain size, η_0, domain formations in the present system are classified into three types; (I) weakly orientated microdomains (x<0.7 mol%;$\eta \approx \eta_0$), (II) composite domain structure of weakly orientated microdomains and large twin-related domains (x=0.9 mol%;$\eta_0 << \eta$), and (III) ideal randomly orientated microdomains (2.0<x<4.4 mol%;$\eta << \eta_0$). Domain sizes are drastically changed by a small amount of water. In addition to the domain formations, we mention the strain in the crystal. It is found that no strain occurs in the crystal lattice at 0-4.4 mol%, since no peak broadening of Bragg reflections along the radial direction (θ-2θ scan mode) was observed in this water concentration range. It is curious that this complicated domain is formed without any intrinsic strain. We wonder whether, in other additives, anomalous type II domains occur. The rocking curves of [DEME][BF_4]-D_2O, -CH_3OH, -C_2H_5OH and -C_6H_6 are shown in Fig. 11(b). The preferred orientations are similar to those at 0.6 (type I) or 2.9 (type III) mol% H_2O. Consequently, we note that the type II domain is limited to the 0.9 mol% H_2O mixture. Therefore, H_2O-mediated hydrogen bonding is peculiar to the crystallization process. It is considered that the Type II domain at 0.9 mol% H_2O mixture is caused by a macroscopic elastic anomaly such as a shape memory effect (Abe et al., 1994).

Not only the domain structure, but also the crystal structure of 0.9 mol% H_2O are obviously different from pure, 0.6 and 2.9 mol% H_2O mixtures (Imai et al., 2009). The orthorhombic lattice of pure [DEME][BF_4] is determined to be a_O=1.012, b_O=1.347, c_O=0.893 nm (Z=4).

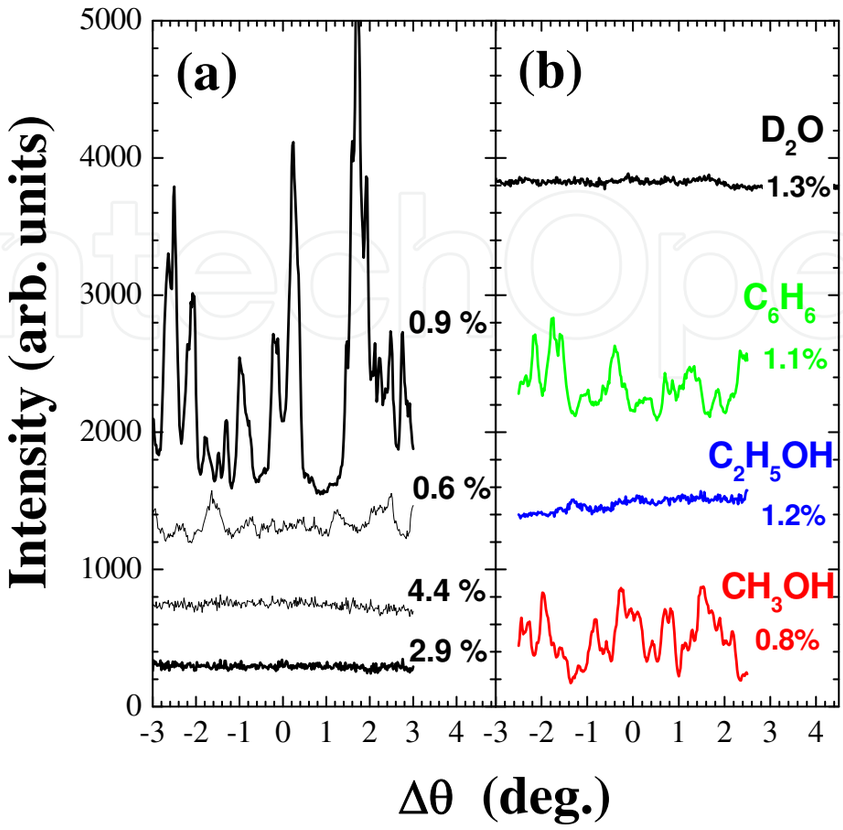

Fig. 11. Rocking curves of (a) H_2O and (b) other additives at -70 °C. Extensive preferred orientation occurs at a specific region of water concentration in [DEME][BF_4]-water mixtures.

WAXS patterns at 0.6, 0.9 and 2.9 mol% H_2O are shown in Fig. 12. If we assume a smaller unit cell and two different kinds of modulated structures (superstructures), the observed 2θ values are almost the same as the calculated ones. The smaller orthorhombic unit cell is expressed by a_O', b_O' and c_O'. Blue circles represent the supercell of $a_O' \times b_O' \times 2c_O'$ (Z=8), while red circles indicate another supercell of $2a_O' \times b_O' \times 2c_O'$ (Z=16) (Fig. 12). Unit cells and the volume per four [DEME][BF_4] units, V_4, of [DEME][BF_4]-H_2O are listed in Table 1. A significant finding is that V_4 at 0.9 mol % is distinctly small. It should be noticed that the twin-related domain at 0.9 mol% H_2O ($\eta_0 << \eta$) is formed with two accompanying kinds of superstructures (Z=4m; m=2 and 4) and a volume contraction (small V_4).

In order to interpret the elastic and structural anomaly at 0.9 mol% H_2O, we introduce a sublattice, which has the equivalent length (2.7 nm) of a sublattice constant, a_{sub}. The sublattice has a peculiar geometric relationship with the orthorhombic lattice (Fig. 13). The lattice relationship is given by,

$$a_{sub} = 2b_O = 3c_O = 2\sqrt{a_O^{\,2} + c_O^{\,2}} \ . \tag{3}$$

The sublattice contains 48 molecules of [DEME][BF_4]. If we assume that one water molecule exists in two sets of sublattices, the elastic anomaly is explained by a water network over the

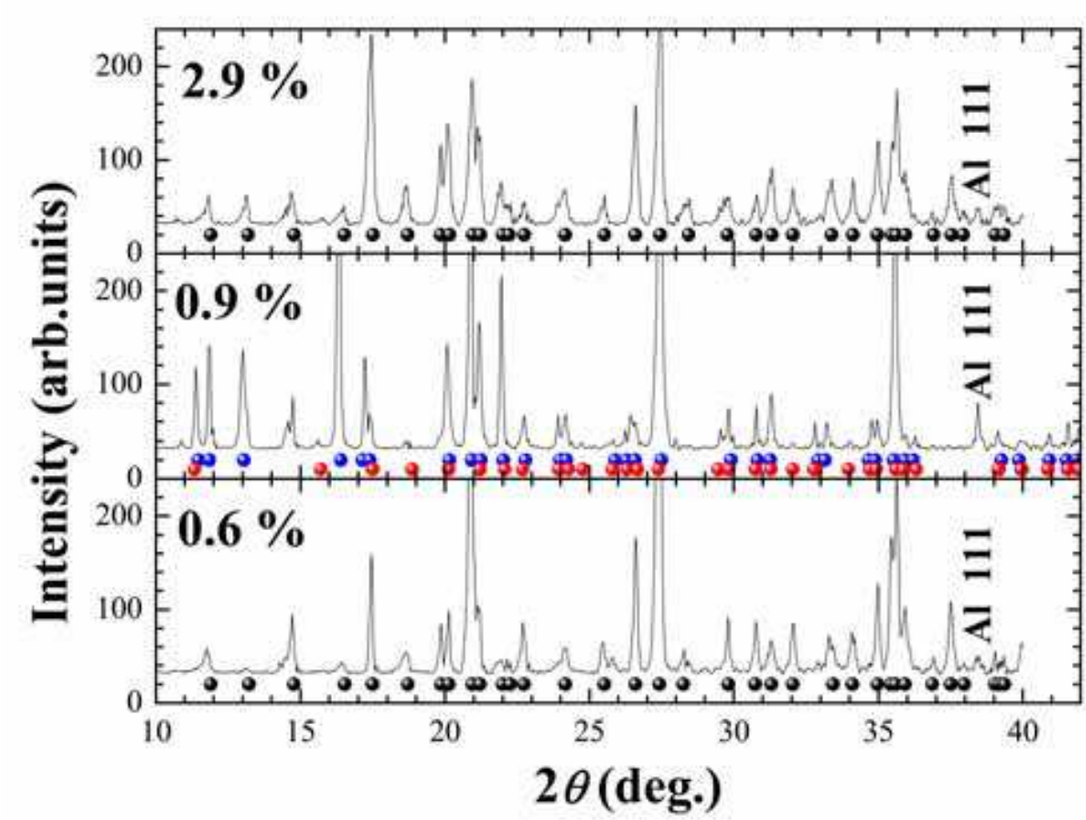

Fig. 12. WAXS patterns of [DEME][BF_4]-H_2O mixtures. Crystal structures of 0.6, 0.9 and 2.9 mol% H_2O are calculated. Only the crystal structure of 0.9 mol % H_2O is not calculated by unit cells of pure [DEME][BF_4]. Blue circles indicate the $a_O' \times b_O' \times 2c_O'$ modulated lattice and red circles indicate the $2a_O' \times b_O' \times 2c_O'$ modulated lattice.

x	Structure	V_4 (nm_3)	T_c
0.6 %	$a_O \times b_O \times c_O$	1.210	-41.5
0.9 %	$a_O' \times b_O' \times 2c_O'$	1.145	-14.4
	$2a_O' \times b_O' \times 2c_O'$	1.101	
2.9 %	$a_O \times b_O \times c_O$	1.210	-45.6
4.4 %	$a_O \times b_O \times c_O$	1.214	-32.8
	$a_O \times b_O \times 2c_O$	1.209	
8.8 %	$a_O \times b_O \times c_O$	1.216	-41.2
12.0 %	$a_O \times b_O \times c_O$	1.219	-50.5

Table 1. Each unit cell in the [DEME][BF_4]-H_2O mixtures is expressed in terms of the lattice constants of pure [DEME][BF_4], where a_O, b_O and c_O indicate those of the orthorhombus. a_O', b_O' and c_O' are smaller lattice constants. V_4 is volume per four molecules (Z=4).

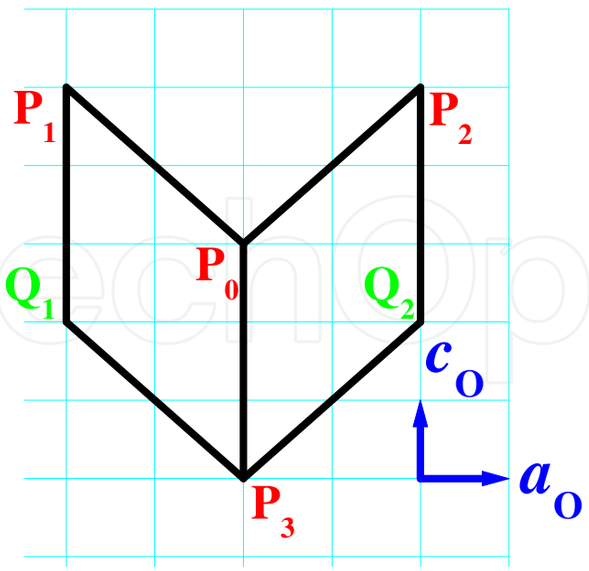

Fig. 13. The geometrical relationship between the orthorhombic lattice and its sublattice is drawn on the a_O–c_O plane. The sublattice is rhombic and the edge length of the rhombus is equal to $2b_O$.

medium-range (Imai et al., 2009). Since the above assumption is defined to be one H_2O molecule and 96 molecules of [DEME][BF_4], 1/(1+96) provides 1.03 mol%. This means that an average distance of 1 mol% additives is equal to the sublattice parameters. The single H_2O molecule in two sets of sublattices is based on the following idea: one molecule can occupy sites at P_1-P_2-Q_1-Q_2, P_0-P_3 and Q_1-Q_2-P_3 on the sublattice points (Fig. 13). Since the lengths of P_0Q_1 and P_0Q_2 are too short, H_2O molecules probably cannot be located at the sublattice points simultaneously. Thus, we consider that the perfect order of H_2O can be realized only at 1 mol%. Also, a medium-range order (MRO) (Abe, 2007b) of H_2O can contribute to the elastic anomaly, supercell and volume contractions at 0.9 mol% H_2O. The geometric effect is enhanced by additions of H_2O, which may be derived from strong hydrogen bonding of H_2O. Recently, water network simulations are carried out by developing this idea (Abe et al., 2010b). The MRO of H_2O is developing in the simulation box.

Our next step is to clarify the anomalous behaviors at 0.9 mol% H_2O by another approach. Since we consider that the anomalies are induced by particular hydrogen bonding of H_2O, we examine the H/D effects at 0.9 mol% H_2O in the same manner as the 'giant isotope effect' of ferroelectrics. In fact, the deuterated effect in RTILs has not been discussed much so far, though various kinds of RTIL-water mixtures have been investigated experimentally and theoretically. By fixing the water concentration at 1 mol%, we prepared [DEME][BF_4]-H_2O, -0.75H_2O·0.25D_2O, -0.5H_2O·0.5D_2O and -D_2O mixtures, where (1-y)H_2O·yD_2O mixtures are provided by the y parameter. We have determined the crystal structures and crystallization temperatures, T_c, of [DEME][BF_4]-H_2O, -0.75H_2O·0.25D_2O, -0.5H_2O·0.5D_2O and -D_2O mixtures by simultaneous WAXS and DSC measurements (Abe et al., 2010a). The T_c, unit cell (Z=4m) and V_4 of the mixtures are revealed in Table 2. It is obvious that T_c decreases with increasing D substitution. Also, superstructures vanish and V_4 increases

	H_2O		$0.75H_2O \bullet 0.25D_2O$	$0.5H_2O \bullet 0.5D_2O$	D_2O
x (mol%)	0.9		1.0	0.9	1.3
T_c (°C)	-14.4		-21.4	-34.8	-39.7
unit cell	$a_O' \times b_O' \times 2c_O'$	$2a_O' \times b_O' \times 2c_O'$	$a_O' \times b_O' \times c_O'$	$a_O \times b_O \times c_O$	$a_O \times b_O \times c_O$
V_4 (nm^3)	1.145	1.101	1.181	1.212	1.209

Table 2. Crystallization temperatures, T_c, unit cells of crystal structures and volume per four molecules (Z=4), V_4, of [DEME][BF_4]-0.9 mol% H_2O, -1.0 mol% $0.75H_2O \cdot 0.25D_2O$, -0.9 mol% $0.5H_2O \cdot 0.5D_2O$ and -1.3 mol% D_2O.

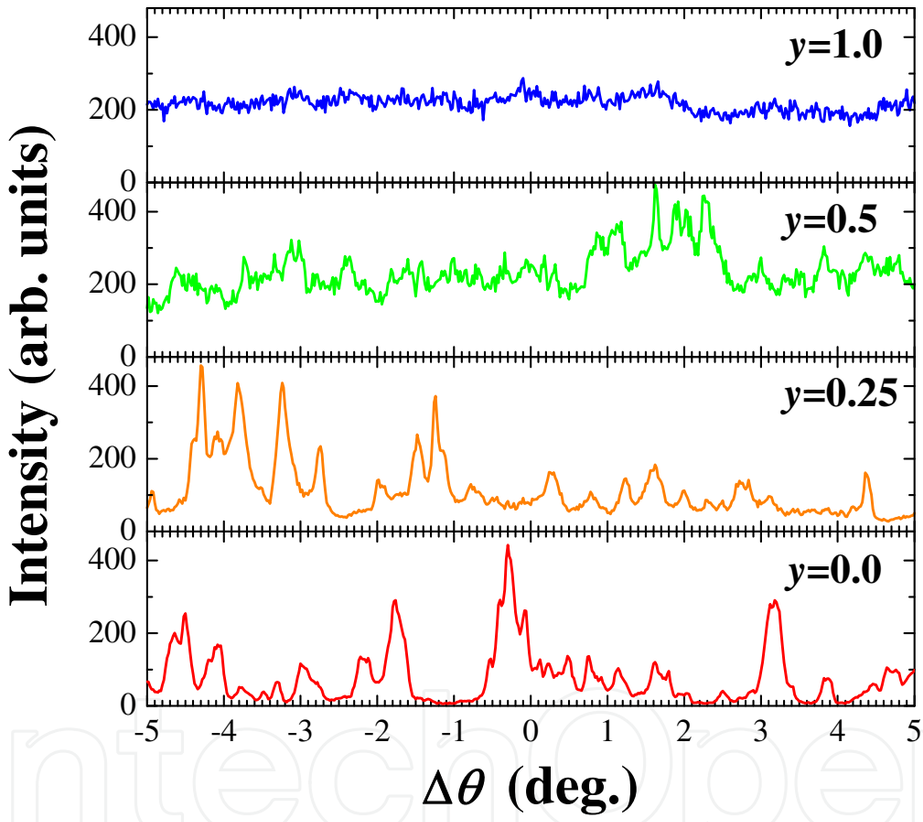

Fig. 14. Rocking curves at -80 °C of [DEME][BF_4]-0.9 mol % H_2O (y=0.0), -1.0 mol % $0.75H_2O \cdot 0.25D_2O$ (y=0.25), -0.9 mol % $0.5H_2O \cdot 0.5D_2O$ (y=0.5) and -1.3 mol % D_2O (y=1.0).

gradually with increasing y. In addition to the θ-2θ scan mode, crystal domain structures of $(1-y)H_2O \cdot yD_2O$ mixtures were examined by θ scan mode. Figure 14 reveals the rocking curves on the Debye rings of the [DEME][BF_4]-0.9 mol% H_2O, -1.0 mol% $0.75H_2O \cdot 0.25D_2O$, -0.9 mol% $0.5H_2O \cdot 0.5D_2O$ and -1.3 mol% D_2O mixtures, respectively. The rocking curves were obtained at a fixed 2θ value (27.4°). In the case of [DEME][BF_4]-0.9 mol% H_2O and -1.0 mol% $0.75H_2O \cdot 0.25D_2O$, an extraordinary highly preferred orientation appears on the Debye ring. Judging from the asymmetric peak profiles or two peak tops, a twin-related domain (Type II; $\eta_0 << \eta$) occurs at y=0.0 and y=0.25. Whereas for the 0.9 mol% $0.5H_2O \cdot 0.5D_2O$

(y=0.5), a conventional preferred orientation is observed. Weak intensity modulations on the Debye ring are expressed by much broader and weaker peaks (Type I; $\eta \approx \eta_0$). Interestingly, the preferred orientation disappears completely in 1.3 mol% D_2O (y=1.0). The domain (y=1.0) that gives an ideal Debye ring corresponds to Type III ($\eta << \eta_0$). Systematically, a very strong H/D effect is obtained in the [DEME][BF_4]-1 mol% water system. The D substitution parameter, y, effects continuous changes of crystallization temperature (T_c), domain structures (η), superstructures (Z=4m) and volume (V_4).

Based on the idea of the protonated effect in KH_2PO (Koval et al., 2002; Koval et al., 2005; Lasave et al., 2005), we assume the hydrogen bonding in the solid, from a microscopic perspective, is as follows: (i) NFHB water in the liquid state might be bound to the F of the anion and also the O of the large cation as shown in Fig. 15(a), once the mixture is

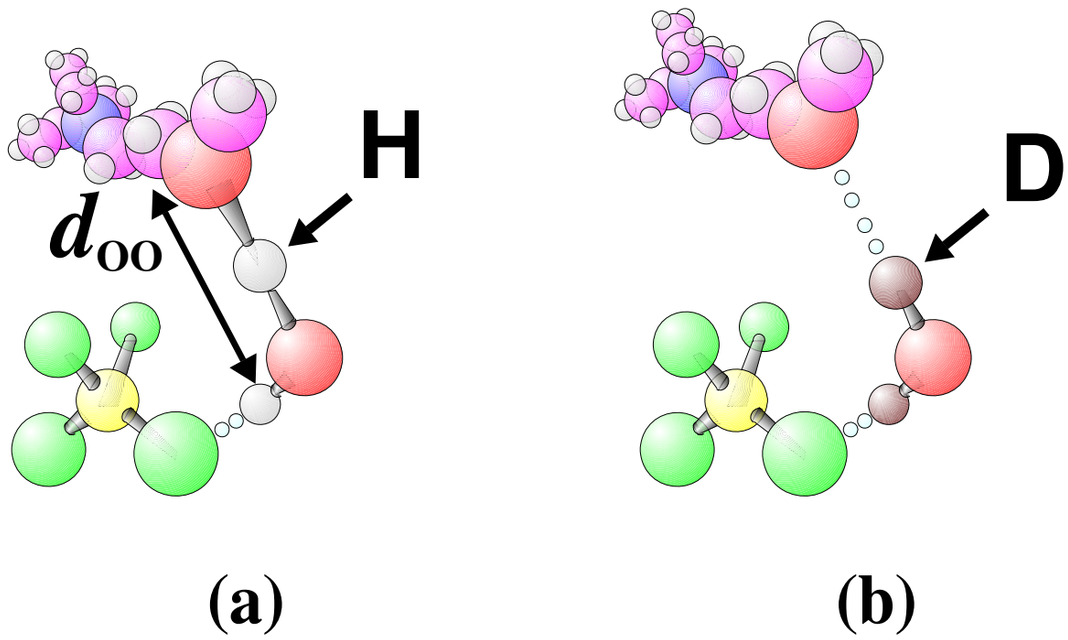

Fig. 15. The bonding scheme of (a) H_2O and (b) D_2O in crystal. In protonated water, 'on-centering' is preferred, whereas 'off-centering' occurs in deuterated water. The atomic distance between oxygens, d_{OO}, varies depending on the interaction.

crystallized by slow cooling. Due to the highly packed solid structure, PMCB (H-O-H) is employed. (ii) D in the solid stays in its off-centered position (O···D-O), as shown in Fig. 15(b). Where there is PMCB (hydrogen delocalization) in the crystal, the atomic distance between O and O, d_{OO}, becomes shorter (Fig. 15(a)), but this attractive interaction does not occur in deuterated water, since the deuteron is stabilized in the off-center position as with KD_2PO_4. From assumption (ii), it follows that associating with deuterated water leads to a larger d_{OO}. We infer that the PMCB in the [DEME][BF_4]-0.9 mol% H_2O crystal causes an extraordinary volume contraction, partly seen in the results in Table 2. A large contribution from PMCB in 1.0 mol % $0.75H_2O \cdot 0.25D_2O$ also provides a small volume contraction. Next, we focus on the influence of D on the domain structure related to PMCB. Domain morphology changes successively with the y parameter as shown in Fig. 14. Using the above PMCB mechanism, the discrepancy of the difference in scale might be resolved. From the

strong H/D effect, we consider that the previously introduced sublattice network is treated as a PMCB perturbation. The geometrical network is a bridge between local atomic shifts (PMCB) and the macroscopic twin-related domain. Similarly, the T_c, which depends on the nucleation process, is connected to the H/D effect. However, the dynamic process connecting the microscopic to the macroscopic still remains unclear. Certainly, it is not sufficient to describe the dynamic motion of the domain wall by WAXS alone. Dynamic properties relating to its local structure could be interpreted from the Raman data, but there is further difficulty of detection with such a small content of water. In fact, we could not detect the differences due to the H/D effects in the Raman spectra at 1 mol % water.

4.5 Hierarchy structure and its relationship to the nearly-free hydrogen bonding in the liquid state

H/D effects on the crystal can lead us to the distinct 'hierarchy' structure based on hydrogen bonding. Considering our experimental results in the liquid state as a whole, the 'hierarchy' of the liquid structure seems to be deeply connected to NFHB water. Figure 16 shows WAXS patterns of [DEME][BF_4]-H_2O mixtures at room temperature. At around 85 mol%, the patterns are modulated differently, and the Q position at the maximum intensity of the principal peak Q_{max} shifts to higher Q (Aono et al., 2011). The same tendency of Q_{max} is seen in [DEME][BF_4]-D_2O mixtures. Q_{max} as a function of H_2O and D_2O concentrations is plotted in Fig. 17. From the viewpoint of H/D effects in the liquid state, the local structure as a function of water concentration does not depend on H_2O or D_2O. Compared with the dense crystal, [DEME][BF_4] and water are loosely bound to each other. The PMCB seen in crystals is not activated in the liquid. The sudden shift of Q_{max} can be regarded as a crossover point, x_c (=85 mol%), to a different liquid structure. In a radial distribution function (RDF) at around 90 mol%, we found that the liquid structure is not represented by a simple superposition of pure [DEME][BF_4] and H_2O (Abe et al., 2010a). This implies that hydrogen bonding is coupled with other factors. In the WAXS, another significant finding was the appearance of a low-Q component such as a 'prepeak' (Allen et al., 1992; Salanne et al., 2008). The intensity of the low-Q component (Q~2 nm^{-1}) increased only between 85 and 95 mol% (Fig. 18). The low-Q component is related to MRO in network-forming ionic liquids, like $ZnCl_2$ or SiO_2. In $ZnCl_2$, voids in the simulated liquid are analyzed using Voronoi polyhedra (Wilson & Madden, 1998). The weak ordering of the voids provides spatial contrast, that is, cation density fluctuations. Generally, the low-Q component is extremely sensitive to the density (Barker et al., 2000). Consequently, the liquid structure in the [DEME][BF_4]-H_2O mixtures has anomalies in coordination number, orientational order and density in the vicinity of 85 mol%.

The liquid structures are roughly divided into three regimes: (i) an RTIL-based structure (x<80 mol%), (ii) an intermediate state (80<x<95 mol%) and (iii) bulk water (95 mol%<x). The intermediate state is not a simple mixing state, but an intrinsically complicated one. For instance, the low-Q component suddenly increases in this region, and RDF analysis indicates that the liquid structure is modified extensively by additional factors. From the viewpoint of molecular configurations, we can discuss the liquid structures in the anomalous mixing state. A simple aggregation of $BF_4^-\cdots n(H_2O)$ as shown in Figs. 9(a), 9(b), 9(c) and 9(d) is preferred below 80 mol%. The optimized arrangements can explain the observed Raman modes in the liquid state well (Takekiyo et al., in preparation.). Since water

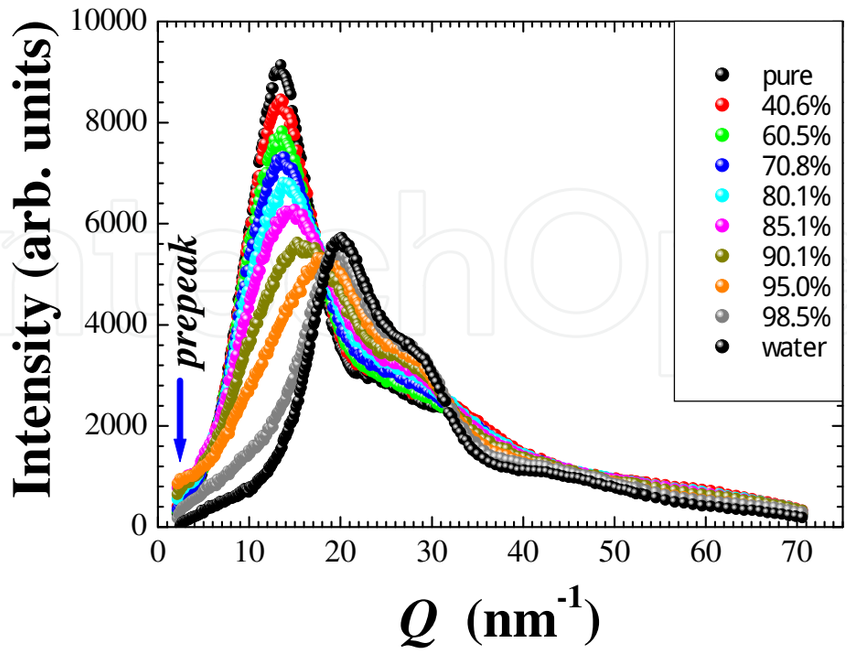

Fig. 16. WAXS intensity changes in [DEME][BF_4]-H_2O mixtures at room temperature. Above 80 mol% H_2O, the maximum position of the normal principal peak in WAXS gradually shifts to that of pure water.

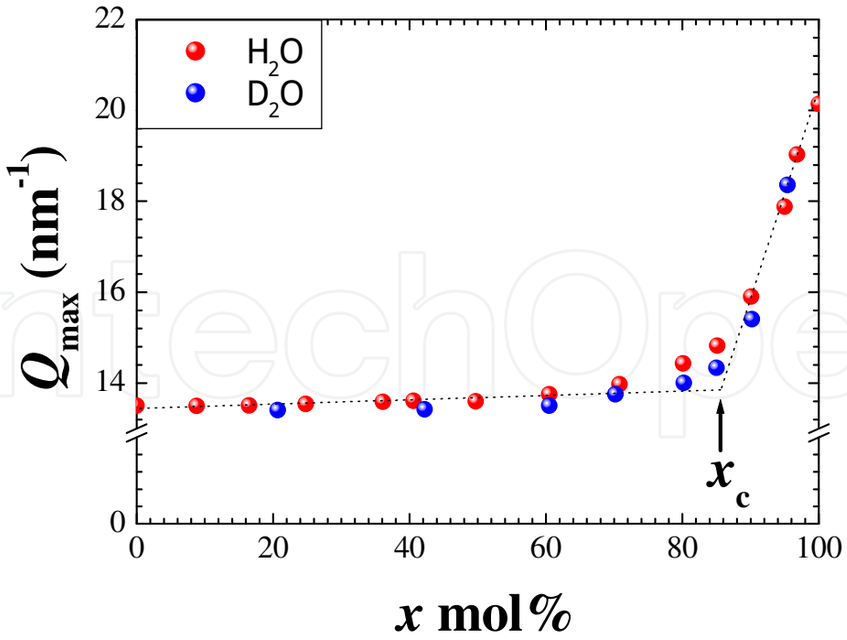

Fig. 17. H_2O and D_2O concentration dependences of Q position at the maximum intensity, Q_{max}, of WAXS patterns (Fig. 16). Q_{max} values increase drastically above 90 mol% H_2O and D_2O.

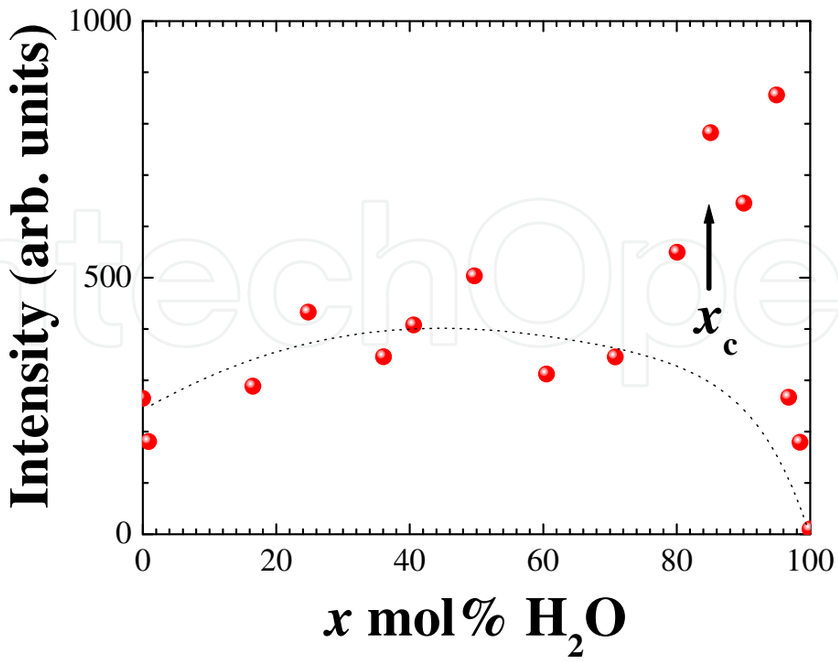

Fig. 18. H_2O concentration dependence of intensity of the low-Q component in WAXS. Q position is 2.1 nm^{-1}, which is provided by the allowances in Fig. 16.

is loosely bound to a BF_4^- anion, bulk water is not formed. This corresponds to the RTIL-based liquid structure below 80 mol%. In contrast, the intermediate scheme with a hierarchy structure requires a new concept, where the idea of $BF_4^-\cdots n(H_2O)$ complexes is developed to interpret the anomalous mixing state at 80-95 mol%.

In order to gather clues about this new concept, SAXS experiments of [DEME][BF_4]-H_2O mixtures were carried out. The SAXS intensity of pure [DEME][BF_4] is relatively strong. The SAXS data do not fit well with representative models such as fractal morphology, lamellar structure, and spinodal decomposition. Therefore, we used the Ornstein-Zernicke (OZ) correlation function in Eq. (2) (Stanley, 1971). The correlation length, ξ, as a function of H_2O concentration was estimated by the OZ correlation function, as shown in Fig. 19. The correlation length of pure [DEME][BF_4] amounts to 1.7 nm in which the large cation size is 0.8 nm. The nanoscale heterogeneity becomes smaller with increasing water content up to 50 mol%. Around 50 mol%, the nanoscale fluctuation almost disappears because the correlation length is almost equal to the cation size. At 65-85 mol%, the correlation length, however, increases again. Finally, the correlation length is suppressed at greater than 90 mol%. The increment of SAXS at 65-85 mol% does not originate from polar and non-polar regions, since the formation of nano-heterogeneity is interrupted by the water network with increasing water concentrations. We confirm that density fluctuations at 65-85 mol% are induced as a precursor phenomenon of the above anomalous mixing state at 80-95 mol%.

In addition to the density fluctuations, the anomalous mixing state of [DEME][BF_4]-H_2O is seen in optical absorption (Aono et al., 2011; Aono et al., submitted). The optical absorption spectra in the UV-vis region are shown in Fig. 20. The absorption spectrum of pure water is provided in the inset of Fig. 20. Pure water has an absorption at 4.7 eV (Laasonen et al., 1993). With an increase in the water content, the optical absorption gradually decreases.

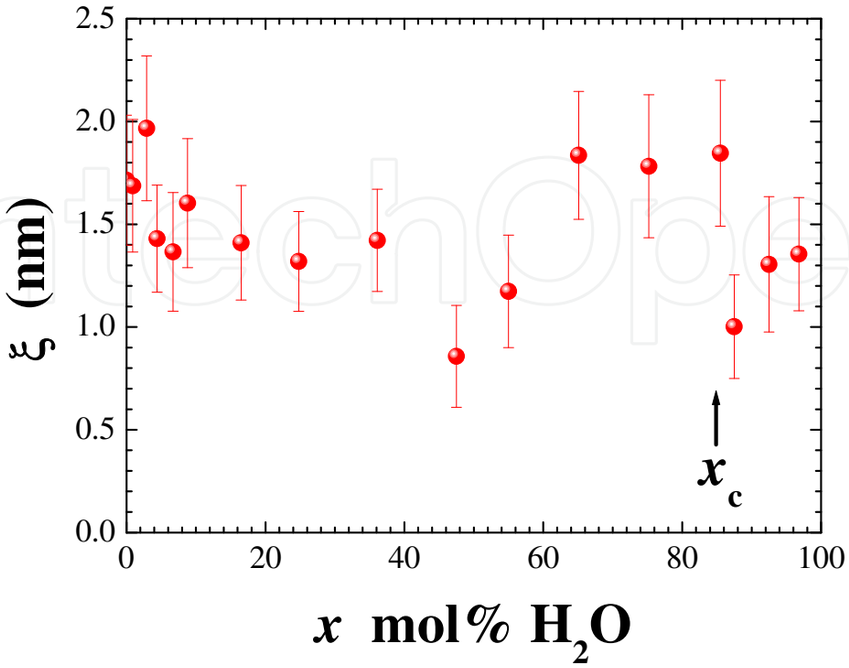

Fig. 19. H_2O concentration dependence of correlation length, ξ, which is obtained with the Ornstein-Zernike correlation function

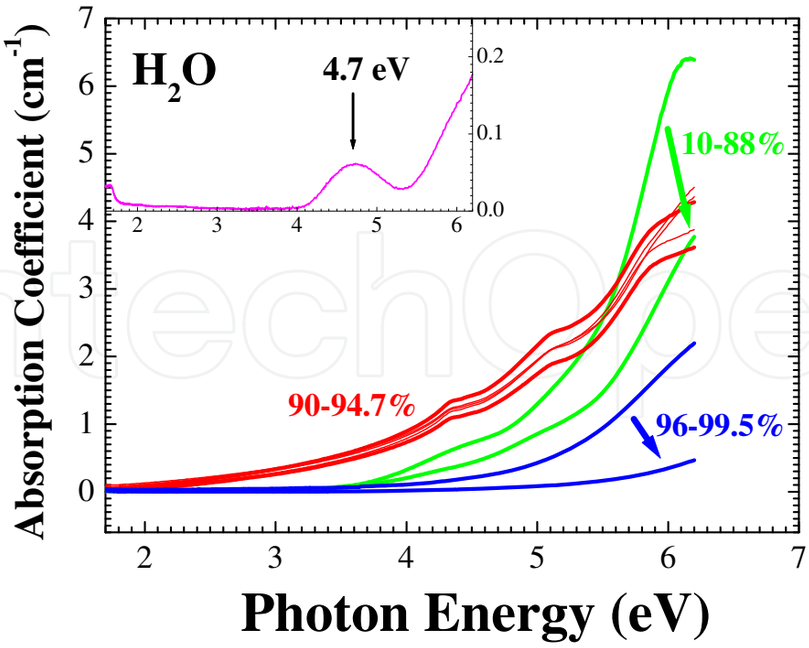

Fig. 20. Optical absorption spectra as a function of water concentration. The inset shows the absorption spectrum of pure water.

However, an unusual increase is seen between 90 and 95 mol%. To see this anomaly, we plot the optical absorption as a function of water concentration in Fig. 21, where the photon energy is fixed at 4.7 eV. Apart from the rapidly increasing region described subsequently, a crossover point in the absorption coefficient, x_c, is observed at 85 mol%. On the simple optical absorption curve, very high absorption appears between 90 and 95 mol%. In a previous study on [C_4mim][PF_6] (Paul et al., 2005), the optical absorption in the UV-vis spectra was explained well. The electronic absorption around 4.4 eV in [C_4mim][PF_6] provides information on the polarity of the RTIL and the dynamics of the diffusion. Here, the possible excited species are induced by the donor-acceptor charge transfer, proton transfer, molecular conformational change, hydrogen bonding ability, and polarity (Mahanta et al., 2008). For the [DEME][BF_4]-H_2O mixture, we focus on the anomalous optical absorption at 90-95 mol%. We introduce the cluster model (Aono et al., submitted), which consists of an inner core and outer shell in an analogy with a micelle structure. The core corresponds to a $BF_4^-\cdots 4(H_2O)$ cluster, based on DFT calculations (Fig.9 (d)). In the outer shell, water molecules are loosely bonded to the inner core. A large cation is excluded from the cluster. The model is not contradicted by the experimentally obtained non-NFHB water above 90 mol%. In the model, four H_2O molecules of the inner core should be hydrogen bonded with outer H_2O molecules.

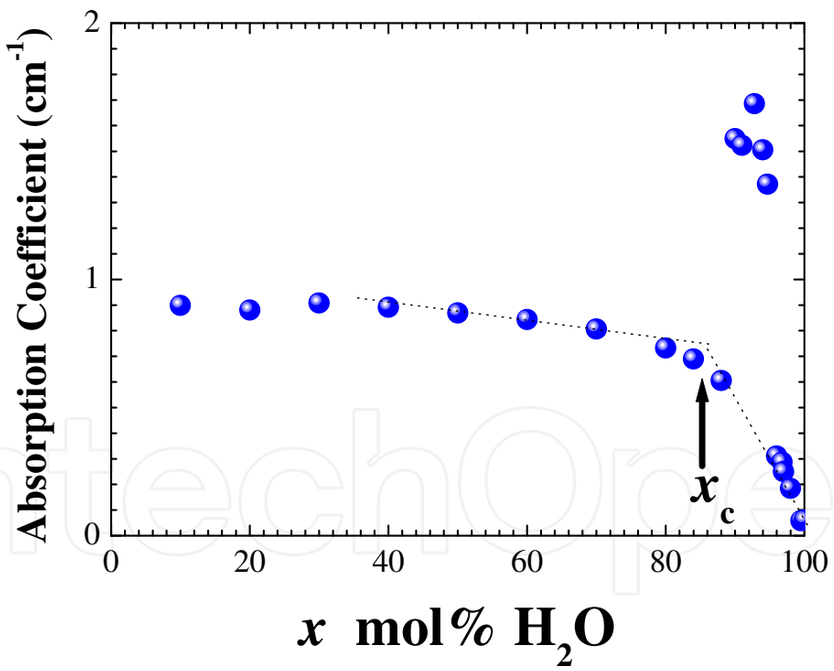

Fig. 21. Water concentration dependence of the optical absorption coefficient at 4.7 eV.

5. Summary

In this study, we explore a variety of water-mediated molecular interactions. Both in the liquid and solid states, the [DEME][BF_4]-H_2O system, a non-imidazolium RTIL, has a lot of phases and states, including a non-equilibrium state. Moreover, some of them are

characterized by self-assembly or hyperstructure. Here, it is crucial that well-organized structure on the mesoscopic scale contributes to the hierarchy. In the case of [DEME][BF_4]-H_2O, hydrogen bonding plays an important role in structural formation at each scale.
The hierarchy structure in the liquid state is summarized in Fig. 22. As an intermediate state between RTIL and bulk water, the hierarchy appears at 80-95 mol%. In order to explain the extraordinary mixing state, we introduce a hybrid cluster (core + shell), which is self-assembled. A core part, described by $BF_4^-\cdots n(H_2O)$, is aggregated by H···F bonding. Non H···F bonding water above 80 mol% surrounds the core part. It is predicted that a (core + shell) cluster has a size distribution and its own relaxation time. Possibly, self-assembled clusters can make a striking contrast in density over the medium-range. If the size of density fluctuations is distributed widely, optical absorption over the whole UV-vis range is recognized by light scattering. We emphasize that the hierarchy of the liquid structure is regarded as one of self-organization based on hydrogen bonding, although there is no H/D effect.

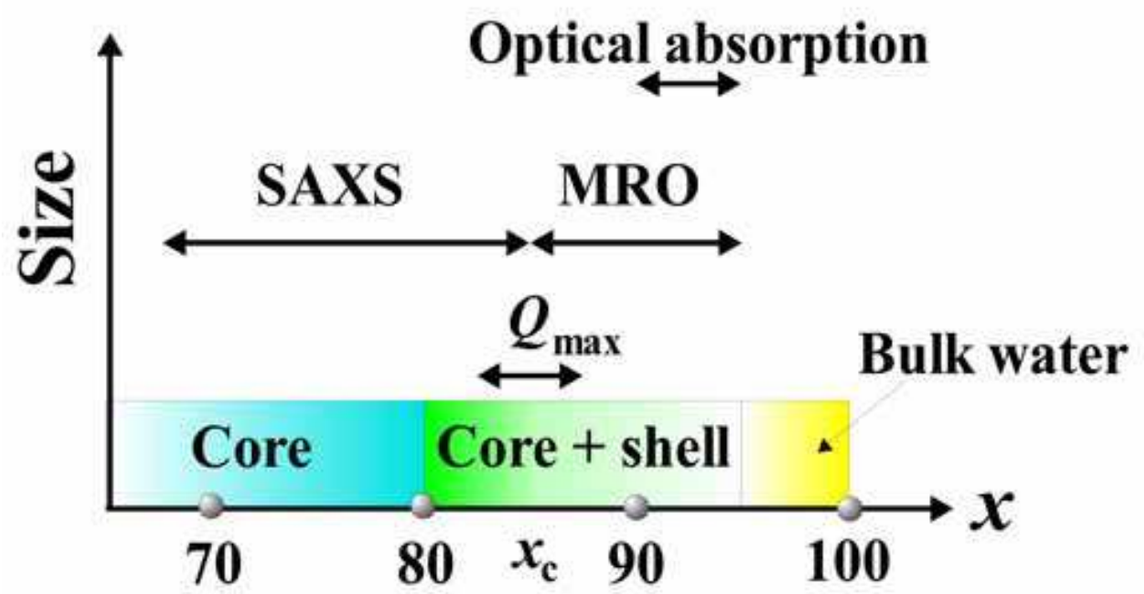

Fig. 22. Hierarchy structure in a liquid state at 80-95 mol% H_2O. MRO (medium-range order) and SAXS (small angle X-ray scattering) reveal density fluctuations at each scale.

In the three different glassy states illustrated in Fig. 10, thermal treatments, heterogeneity and NFHB can distinguish the glass forming mechanism. In the denser solid state, hydrogen bonding effectively acts on the glasses instead of forming a non-equilibrium state. The big difference in hydrogen bonding is described by the non-NFHB of slow-cooled glasses and NFHB of quenched ones. Furthermore, a double glass transition is observed in the quenched glass, which is formed extremely far from an equilibrium state. Freezing separately into water-poor and water–rich regions proves that there are two kinds of water roles. In the water-rich region, T_{g2} becomes higher alongside a change to hard glass, where water molecules act as binding between other molecules. On the other hand, water-poor glass is unstable, with lower T_{g1}. In the soft glass of the water-poor region, water molecules tend conversely to break the glassy state. Hence, heterogeneity (water-rich + water–poor) formed

by the two different roles of water is distinguished from the nano-heterogeneity (polar + non-polar) of pure RTILs. Since ΔT_g in the double glass transition is quite small, each region of water-rich and water–poor is estimated to be relatively small. Therefore, coexistence of hard and soft glasses in the double glass transition is regarded as a kind of hierarchic anomaly related to macroscopic glass transition temperatures.

In the crystal state, at 1 mol% H_2O only, macroscopic anomalies are observed. The anomalies are as follows; (i) high crystallization temperature (T_c), (ii) twin-related domain ($\eta >> \eta_0$), (iii) superstructures ($Z=4m$) and (iv) volume contraction (small V_4). In proportion to D substitution, these anomalies gradually disappear. The H/D effect reveals that H is extensively involved in hydrogen bonding despite the small amount of water. The inherent bonding nature of H is explained by introducing attractive PMCB on the microscopic scale (Abe et al., 2010a) and repulsive water in the sublattice network (Abe et al., 2010b) (Fig. 23). If just 1 mol% of water is fully ordered on the sublattice with an equivalent sublattice constant, the geometrical order provides an elastic influence on the whole lattice. The mutual effects of the virtual PMCB and sublattice network become more realistic with strong H/D effects.

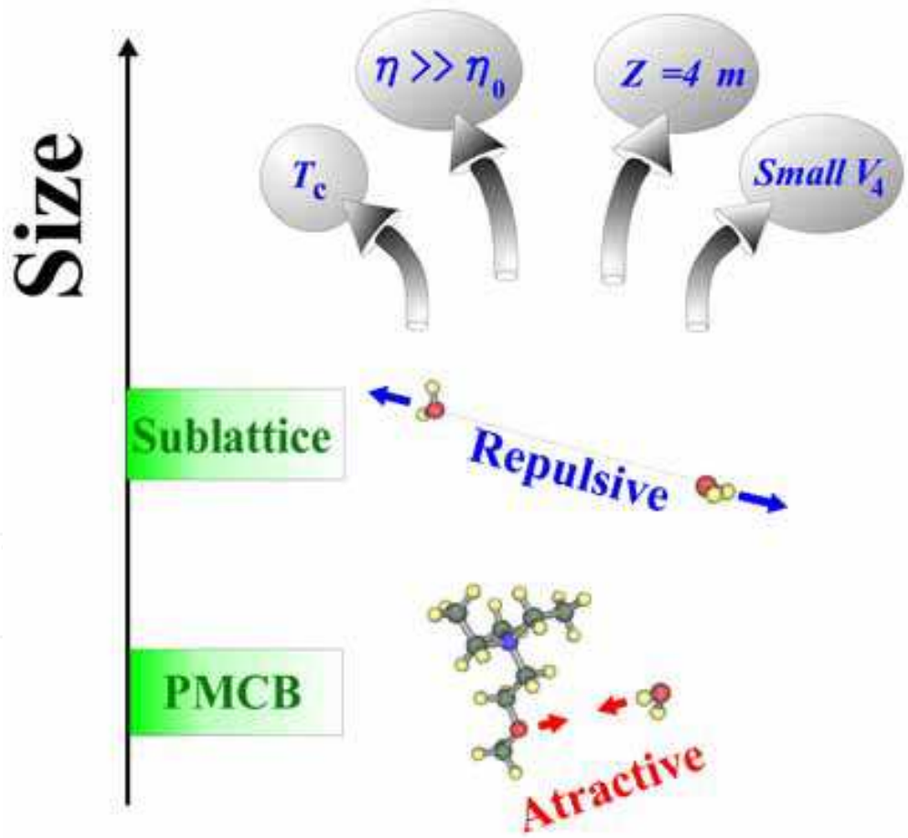

Fig. 23. Hierarchy structure of crystals at 1 mol% H_2O. Proton-mediated covalent bonding (PMCB) controls macroscopic properties such as crystallization temperature, T_c, twin-related domain ($\eta >> \eta_0$), superstructures ($Z=4m$) and volume contraction (V_4). The H/D effect is dominant only at 1 mol% H_2O.

A water molecule can bring out hidden properties of other molecules. For instance, proteins fully utilize the effects of water molecules. To understand the hydrogen bonding of water geometrically is significant for clarifying its 'function and structure'. The grouping of hydrogen bonding has just begun in simple molecular systems such as [DEME][BF_4]-H_2O.

6. Acknowledgements

We appreciate Ms. M. Yasaka and Mr. A. Kishi of Rigaku Co. for experimental support and helpful discussions. Also, the authors sincerely thank Mr. Y. Imai, Mr. T. Goto of National Defense Academy for experimental support. Dr. M. Aono and Dr. T. Takekiyo are our collaborators and some experimental results were obtained by them. Also, we provide special thanks to Prof. N. Hamaya of Ochanomizu University, Prof. A. Shimizu of Soka University, Professor H. Matsumoto and Professor T. Arai of National Defense Academy for helpful discussions.

7. References

Abe, H., Ishibashi, M., Ohshima, K., Suzuki, T., Wuttig, M. & Kakurai, K. (1994) Kinetics of martensitic transition in In-Tl alloys, *Phys. Rev. B* Vol. 50: 9020-9024.

Abe, H., Yamamoto, K., Matsuoka, S. & Matsuo, Y. (2007a) Atomic short-range order in an $Al_{72}Ni_{18}Fe_{10}$ decagonal quasicrystal studied by anomalous x-ray scattering, *J. Phys.: Condens. Matter* Vol. 19: 466201-14.

Abe, H. (2007b) Reverse Monte Carlo Modeling of Local Structure Using Short-Range and Medium-Range Order Parameters, *J. Phys. Soc. Jpn.* Vol. 76: 094601-6.

Abe, H., Yoshimura, Y., Imai, Y., Goto, T. & Matsumoto, H. (2009) Phase behavior of room temperature ionic liquid-H_2O mixtures: *N*, *N*-diethyl-*N*-methyl-N-2-methoxyethyl ammonium tetrafluoroborate, *J. Mol. Liq.* Vol. 150: 16-21.

Abe, H., Imai, Y., Takekiyo, T. & Yoshimura, Y. (2010a) Deuterated Water Effect in a Room Temperature Ionic Liquid: *N*,*N*-Diethyl-*N*-methyl-*N*-2-methoxyethyl Ammonium Tetrafluoroborate, *J. Phys. Chem. B* Vol. 114 : 2834-2839.

Abe, H., Imai, Y., Goto, T., Yoshimura, Y., Aono, M., Takekiyo, T., Matsumoto, H. & Arai, T. (2010b) Water Network in Room-Temperature Ionic Liquid: *N*, *N*-Diethyl-*N*-Methyl-*N*-2-Methoxyethyl Ammonium Tetrafluoroborate, *Metal. Mater. Trans. A* Vol. 41: 1137-1143.

Allen, D. A., Howe, R. A., Wood, N. D. & Howells, W. S. (1992) The structure of molten zinc chloride and potassium chloride mixtures, *J. Phys.: Condens. Matter* Vol. 4: 1407-1418.

Aono, M., Imai, Y., Ogata, Y., Abe, H., Goto, T., Yoshimura, Y., Takekiyo, T., Matsumoto, H. and Arai, T. (2011) Anomalous Mixing State in Room-Temperature Ionic Liquid-Water Mixtures: *N*, *N*-diethyl-*N*-methyl-*N*-(2-methoxyethyl) Ammonium Tetrafluoroborate, *Metal. Mater. Trans*., Vol. 42A: 37-40.

Aono, M., Imai, Y., Abe, H., Matsumoto, H. & Yoshimura, Y., Optical Interaction of Room Temperature Ionic Liquid- Water Mixtures : *N*, *N*-diethyl-*N*-methyl-*N*- (2-methoxyethyl) Ammonium Tetrafluoroborate, submitted to Thermochim. Acta.

Barker, D. R., Wilson, M., Madden, P. A., Medvedev, N. N. & Geiger, A. (2000) Voids in the H-bonded network of water and their manifestation in the structure factor, *Phys. Rev. E* Vol. 62: 1427-1430.

Becke, A. D. (1988) Density-functional exchange-energy approximation with correct asymptotic behavior, *Phys. Rev. A* Vol. 38: 3098-3100.

Danten, Y., Cabaço, M. I. & Besnard, M. (2010) Interaction of water diluted in 1-butyl-3-methyl imidazolium ionic liquids by vibrational spectroscopy modeling, *J. Mol. Liq.* Vol. 153: 57-66.

Foces-Foces, C., Echevarria, A., Jagerovic, N., Alkorta, I., Elguero, J., Langer, U., Klein, O., Minguet-Bonvehi, M. & Limbach, H-. (2001) A Solid-State NMR, X-ray Diffraction, and ab Initio Computational Study of Hydrogen-Bond Structure and Dynamics of Pyrazole-4-Carboxylic Acid Chains, *J. Am. Chem. Soc.* Vol. 123: 7898-7906.

Frish, M. J.; Trucks, G. W.; H.B. Schlegel, G. E.; Scuseria, M. A.; Robb, J. R.; Cheeseman, V. G.; Zakrzewski, J. A.; Montogomery, A. D.; Daniels, K. N.; Kudin, M. C.; Strain, O.; Farkas, J.; Tomasi, V.; Barone, M.; Cossi, R.; Cammi, B.; Mennucci, C.; Pomelli, C.; Adamo, S.; Clifford, J.; Ochterski, G. A.; Petersson, P. Y.; Ayala, Q. Cui, Morokuma, K.; Malick, D. K.; Rabuck, A. D.; Raghavechari, K.; Foresman, J. B.; Cioslowski, J.; Ortiz, J. V.; Baboul, A. G..; Stefanov, B. B.; Liu, G.; Liashenko, A.; Piskorz, P.; Komaromi, I.; Gomperts, R.; Martin, R. L.; Fox, D. J.; Kieth, T.; Al-Laham, M. A.; Peng, C. Y. ;Nanayaakkara, A.; Gonzalez, C.; Challacombe, M. P.; Gill, M.W.; Johnson, B.; Chen, W.; Wong M. W.; Andres, J. L.; Gonzalez, C.; Head-Gordon, M.; Replogle, E.S.; Pople, J. A. *(*2003) *GAUSSIAN 03*, Gaussian, Inc., Pittsburgh, PA,.

Imai, Y., Abe, H., Goto, T., Yoshimura, Y., Michishita, Y. & Matsumoto, H. (2008a) Structure and thermal property of *N*, *N*-diethyl-*N*-methyl-*N*-2-methoxyethyl ammonium tetrafluoroborate-H_2O mixtures, *Chem. Phys.* Vol. 352: 224-230.

Imai, Y., Abe, H., Goto, T., Yoshimura, Y., Kushiyama, S. & Matsumoto, H. (2008b) Orientational Ordering of Crystal Domains in Ionic Liquid Based Mixtures, *J. Phys. Chem. B* Vol. 112: 9841-9846.

Imai, Y., Abe, H. & Yoshimura, Y. (2009) X-ray Diffraction Study of Ionic Liquid Based Mixtures, *J. Phys. Chem. B* Vol. 113: 2013-2018.

Imai, Y., Abe, H., Miyashita, T., Goto, T. Matsumoto, H. & Yoshimura, Y. (2010) Two glass transitions in *N*, *N*-diethyl-*N*-methyl-*N*-(2-methoxyethyl) ammonium tetrafluoroborate-H_2O mixed solutions, *Chem. Phys. Lett.* Vol. 486: 37-39.

Imai, Y., Abe, H., Matsumoto, H., Shimada, O., Hanasaki, T. & Yoshimura, Y. (2011) Glass Transition Behavior of the Quaternary Ammonium Type Ionic Liquid, [DEME][I]-H_2O Mixtures, J. Chem. Thermodynamics, in press.

Inaba, A. & Andersson, O. (2007) Multiple glass transitions and two step crystallization for the binary system of water and glycerol, *Thermochim. Acta* Vol. 461: 44-49.

Jiang, W., Wang, Y. & Voth, G. A. (2007) Molecular Dynamics Simulation of Nanostructural Organization in Ionic Liquid/Water Mixtures, *J. Phys. Chem. B* Vol. 111: 4812-4818.

Kanno, H., Shimada, K. & Katoh, K. (1983) Two glass transitions in the tetraethylammonium chloride—water system: Evidence for a metastable liquid—liquid immiscibility at low temperatures, *Chem. Phys. Lett.* Vol. 103*:* 219-221.

Katayanagi, H., Hayashi, S., Hamaguchi, H. & Nishikawa, K. (2004) Structure of an ionic liquid, 1-n-butyl-3-methylimidazolium iodide, studied by wide-angle X-ray scattering and Raman spectroscopy, Chem. Phys. Lett. Vol. 392: 460-464.

Klein, O., Aguilar-Parrilla, F., Lopez, J., Jagerovic, N., Elguero, J. & Limbach, H-H. (2004) Dynamic NMR Study of the Mechanisms of Double, Triple, and Quadruple Proton and Deuteron Transfer in Cyclic Hydrogen Bonded Solids of Pyrazole Derivatives, *J. Am. Chem. Soc.* Vol. 126: 11718-11732.

Koval, S., Kohanoff, J., Migoni, R. L. & Tosatti, E. (2002) Ferroelectricity and Isotope Effects in Hydrogen-Bonded KDP Crystals, *Phys. Rev. Lett.* Vol. 89: 187602-4.

Koval, S., Kohanoff, J., Lasave, J., Colizzi, G. & Migoni, R. L. (2005) First-principles study of ferroelectricity and isotope effects in H-bonded KH_2PO_4 crystals, Phys. Rev. B Vol. 71: 184102-15.

Kumar, P., Yan, Z., Xu, L., Mazza, M. G., Buldyrev, S.V., Chen, S.-H., Sastry S. & Stanley, H. E. (2006) Glass Transition in Biomolecules and the Liquid-Liquid Critical Point of Water, *Phys. Rev. Lett.* Vol. 97: 177802-4.

Laasonen, K., Sprik, M., Parrinello, M. & Car, R. (1993) 'Ab initio" liquid water, *J. Chem. Phys.* Vol. 99: 9080-9089.

Lasave, J., Koval, S., Dalal N. S. & Migoni R. L. (2005) Slater and Takagi defects in KH_2PO_4 from first principles, *Phys. Rev. Lett. B* Vol. 72: 104104-8.

Lee, C., Yang, W. & Parr, R. G. (1988) Development of the Colle-Salvetti correlation-energy formula into a functional of the electron density, *Rhys. Rev. B* Vol. 37: 785-789.

Mahanta, S., Singh, R. B., Kar, S. & Guchhait, N. (2008) Evidence of coupled photoinduced proton transfer and intramolecular charge transfer reaction in para-N,N-dimethylamino orthohydroxy benzaldehyde: Spectroscopic and theoretical studies, Chemical Physics Vol. 354: 118-129.

Marechal, Y. (2007). *The Hydrogen Bond and the Water Molecule*, Elsevier, Amsterdam.

Mishima, O. & Stanley, H. E. (1998) The relationship between liquid, supercooled and glassy water, *nature* Vol. 396: 329-335.

Nishikawa, K. & Iijima, T. (1984) Corrections for Intensity Data in Energy-dispersive X-Ray Diffractometry of Liquids. Application to Carbon Tetrachloride, *Bull. Chem. Soc. Jpn*. Vol. 57: 1750-1759.

Paul, A., Mandal, P.K. & Samanta A. (2005) How transparent are the imidazolium ionic liquids? A case study with 1-methyl-3-butylimidazolium hexafluorophosphate, [bmim][PF_6], Chem. Phys. Lett. Vol. 402: 375-379.

Salanne, M., Simon, C., Turq, P. & Madden, P. A. (2008) Intermediate range chemical ordering of cations in simple molten alkali halides, *J. Phys.: Condens. Matter* Vol. 20: 2101-5.

Salzmann, C. G., Radaelli, P. G., Mayer, E. & Finney, J. L. (2009) Ice XV: A New Thermodynamically Stable Phase of Ice, *Phys. Rev. Lett.* Vol. 103: 105701-4.

Sato, T., Masuda, G. & Takagi, K. (2004) Electrochemical properties of novel ionic liquids for electric double layer capacitor applications, *Electrochim. Acta* Vol. 49: 3603-3611.

Satoh, T., Goldfarb, R. B. & Patton, C. E. (1978) Exchange-anisotropy field in disordered nickel-manganese alloys, *J. Appl. Phys.* Vol. 49: 3439-3453.

Stanley H. E. (1971) *Introduction to phase Transition and Critical Phenomena*, Oxford University Press.

Takekiyo, T., Yoshimura, Y., Imai, Y. & H. Abe, in preparation.

Triolo, A., Russina, O., Bleif, H-J. & Cola, E. D. (2007) Nanoscale Segregation in Room Temperature Ionic Liquids, *J. Phys. Chem. B* Vol. 111: 4641-4644.

Yoshimura, Y., Goto, T., Abe, H. & Imai, Y. (2009) Existence of Nearly-Free Hydrogen Bonds in an Ionic Liquid, *N*, *N*-Diethyl-*N*-methyl-*N*-(2-methoxyethyl) Ammonium Tetrafluoroborate-Water at 77 K, *J. Phys. Chem. B* Vol. 113: 8091-8095.

Yoshimura, Y., Kimura, H., Okamoto, C., Miyashita, T., Imai, Y. and H. Abe, (2011) Glass transition behavior of ionic liquid, 1-butyl-3-methylimidazolium tetrabluoroborate-H_2O mixed solutions, J. Chem. Thermodynamics, in press.

Wilson, M. & Madden, P. A. (1998) Voids, Layers, and the First Sharp Diffraction Peak in $ZnCl_2$, *Phys. Rev. Lett.* Vol. 80: 532-535, in press.

Zhang, L., Xu, Z., Wang, Y. & Li, H. (2008) Prediction of the Solvation and Structural Properties of Ionic Liquids in Water by Two-Dimensional Correlation Spectroscopy, *J. Phys. Chem. B* Vol. 112: 6411-6419.

Ionic Liquids: Theory, Properties, New Approaches
Edited by Prof. Alexander Kokorin

ISBN 978-953-307-349-1
Hard cover, 738 pages
Publisher InTech
Published online 28, February, 2011
Published in print edition February, 2011

Ionic Liquids (ILs) are one of the most interesting and rapidly developing areas of modern physical chemistry, technologies and engineering. This book, consisting of 29 chapters gathered in 4 sections, reviews in detail and compiles information about some important physical-chemical properties of ILs and new practical approaches. This is the first book of a series of forthcoming publications on this field by this publisher. The first volume covers some aspects of synthesis, isolation, production, modification, the analysis methods and modeling to reveal the structures and properties of some room temperature ILs, as well as their new possible applications. The book will be of help to chemists, physicists, biologists, technologists and other experts in a variety of disciplines, both academic and industrial, as well as to students and PhD students. It may help to promote the progress in ILs development also.

INTECH
open science | open minds

InTech Europe
University Campus STeP Ri
Slavka Krautzeka 83/A
51000 Rijeka, Croatia
Phone: +385 (51) 770 447
Fax: +385 (51) 686 166
www.intechopen.com

InTech China
Unit 405, Office Block, Hotel Equatorial Shanghai
No.65, Yan An Road (West), Shanghai, 200040, China
中国上海市延安西路65号上海国际贵都大饭店办公楼405单元
Phone: +86-21-62489820
Fax: +86-21-62489821

IntechOpen